

REPORT DOCUMENTATION PAGE

Form Approved
OMB No. 0704-0188

Public reporting burden for this collection of information is estimated to average 1 hour per response, including the time for reviewing instructions, searching existing data sources, gathering and maintaining the data needed, and completing and reviewing this collection of information. Send comments regarding this burden estimate or any other aspect of this collection of information, including suggestions for reducing this burden to Department of Defense, Washington Headquarters Services, Directorate for Information Operations and Reports (0704-0188), 1215 Jefferson Davis Highway, Suite 1204, Arlington, VA 22202-4302. Respondents should be aware that notwithstanding any other provision of law, no person shall be subject to any penalty for failing to comply with a collection of information if it does not display a currently valid OMB control number. **PLEASE DO NOT RETURN YOUR FORM TO THE ABOVE ADDRESS.**

1. REPORT DATE (DD-MM-YYYY) 02/28/2012		2. REPORT TYPE Final Performance Report		3. DATES COVERED (From - To) 2/15/2009-11/30/2011	
4. TITLE AND SUBTITLE Bio-Inspired Integrated Sensing and Control Flapping Flight for Micro Aerial Vehicles				5a. CONTRACT NUMBER FA9550-09-1-0089	
				5b. GRANT NUMBER FA9550-09-1-0089	
				5c. PROGRAM ELEMENT NUMBER	
6. AUTHOR(S) Soon-Jo Chung				5d. PROJECT NUMBER	
				5e. TASK NUMBER	
				5f. WORK UNIT NUMBER	
7. PERFORMING ORGANIZATION NAME(S) AND ADDRESS(ES) University of Illinois at Urbana-Champaign 104 S. Wright St, 306 Talbot Lab, Urbana, IL 61801-2935				8. PERFORMING ORGANIZATION REPORT NUMBER N/A	
9. SPONSORING / MONITORING AGENCY NAME(S) AND ADDRESS(ES) AF Office of Scientific Research 875 N. Randolph St. Room 3112 Arlington, VA 22203				10. SPONSOR/MONITOR'S ACRONYM(S) AFOSR	
				11. SPONSOR/MONITOR'S REPORT NUMBER(S) AFRL-OSR-VA-TR-2012-0349	
12. DISTRIBUTION / AVAILABILITY STATEMENT Distribution A: Approved for Public Release					
13. SUPPLEMENTARY NOTES					
14. ABSTRACT This AFOSR YIP project provides a comprehensive understanding of the unique dynamics and control characteristics of tailless micro aerial vehicle equipped with flexible, articulated wings. This project has successfully demonstrated the ability to stabilize and control the robotic flapping testbed by using the phase synchronized nonlinear oscillators inspired by the central pattern generators in spinal cord. Furthermore, it is shown that the dihedral angle of the wing can be varied symmetrically to obtain an additional degree of freedom, namely, the ability to change flight path angle independently of the flight speed. Asymmetric dihedral settings can be used to perform rapid turns and control the sideslip. From the standpoint of control, the most important observation was the discovery of maneuver-dependent control effectiveness reversal. Successful closed-loop demonstrations of agile maneuvers are presented by using the micro aerial vehicle equipped with articulated wings. Finally, this project reports the first rigorous derivation and simulation results of PDE-based control laws for controlling the deformation of flexible wings to achieve a net aerodynamic force or moment. The controller designed for wing bending employs a novel idea based on splitting a perturbation-observer into two parts: one accommodates the external forces and the other accommodates the boundary control.					
15. SUBJECT TERMS					
16. SECURITY CLASSIFICATION OF:			17. LIMITATION OF ABSTRACT	18. NUMBER OF PAGES	19a. NAME OF RESPONSIBLE PERSON
a. REPORT	b. ABSTRACT	c. THIS PAGE			19b. TELEPHONE NUMBER (include area code) 217-244-2737

Bio-Inspired Integrated Sensing and Control of Flapping Flight for Micro Aerial Vehicles

Soon-Jo Chung, Sc.D., University of Illinois at Urbana-Champaign
Program Monitor: Dr. Willard Larkin

Executive Summary

There is a considerable interest in developing robotic aircraft, inspired by birds, for a variety of missions covering reconnaissance and surveillance. Flapping wing micro aerial vehicle (MAV) concepts have been put forth in light of the efficiency of flapping flight at small scales. These aircraft are naturally equipped with the ability to rotate their wings about the root, a form of wing articulation. This AFOSR Young Investigator Program (YIP) project covers comprehensive research problems concerning the performance, stability and control of tailless robotic aircraft with articulated wings in flapping and gliding flight.

Neurobiologically Inspired Control of Flapping Flight. Significant progress has been made in developing a rigorous mathematical model of a neurobiologically inspired in the form of central pattern generators to control flapping-flight dynamics. A rigorous mathematical and control theoretic framework to design complex three-dimensional wing motions has been developed based on phase synchronization of nonlinear oscillators. In particular, this work shows that flapping-flying dynamics without a tail or traditional aerodynamic control surfaces can be effectively controlled by a reduced set of central pattern generator parameters that generate phase-synchronized or symmetry-breaking oscillatory motions of two main wings. Furthermore, by using Hopf bifurcation, this work shows that tailless aircraft alternating between flapping and gliding can be effectively stabilized by smooth wing motions driven by the central pattern generator network. This work, published in the *AIAA Journal of Guidance, Control, and Dynamics*, was awarded the Best Paper Award from the AIAA Infotech @ Aerospace Conference in 2009 [J1]. Another contribution of this AFOSR-funded research is to investigate at the transient behaviors between flapping and gliding motions of birds. In contrast with small insects or humming birds, birds do glide and perch by controlling their articulated wings. New insights have been derived into how birds or bats without a vertical tail can stabilize and control their agile motions [J2,J3]. This part of research is essential to realize a bat-sized MAV that has to alternate between flapping and gliding for lower-energetic costs and perching maneuvers. In contrast with other ongoing research projects in flapping flight of an insect-like MAV, flapping flying MAVs whose size are similar to that of birds and bats are developed for this project, with an aim to demonstrate closed-loop experimentation of engineered flapping flight. A robotic bat with 8 motors has been developed and installed on a 3-DOF pendulum [B1]. This AFOSR project successfully demonstrated that complicated flapping dynamic motions could be controlled by using phase synchronization of CPG oscillators by using this robotic bat testbed.

Dynamics and Performance of Articulated-Wing Aircraft. The dynamics of articulated-winged MAVs without a vertical tail has been studied in detail [J2,J3,B1]. This work shows that how birds can effectively control its dihedral angles in gliding flight to stabilize their lateral motions without a vertical tail. Although the dynamics and control of articulated wing aircraft share several common features with conventional fixed wing aircraft, the presence of wing articulation presents

several unique benefits as well as limitations from the perspective of performance and control. One of the objectives of this AFOSR project is to understand these features using a combination of theoretical and numerical tools. The aircraft concept envisioned in this project uses the wing dihedral angles for longitudinal and lateral-directional control. Aircraft with flexible articulated wings are also investigated. A complete nonlinear model of the flight dynamics incorporating dynamic Center of Gravity (CG) location and the changing moment of inertia has been derived. It is shown that symmetric dihedral configuration, along with a conventional horizontal tail, can be used to control flight speed and flight path angle independently of each other. This characteristic is very useful for initiating an efficient perching maneuver. Experimental results [B1,J5] are presented which help demonstrate the capability of wing dihedral for control and for executing maneuvers such as slow, rapid descent and perching. Both open-loop and closed-loop experiments with the Cgull articulated-wing MAV were performed to demonstrate (a) the effectiveness of symmetric dihedral for flight path angle control, (b) yaw control using asymmetric dihedral, and (c) the elements of perching.

Dynamics and Control of Aircraft with Flexible, Articulated Wings. It is shown that wing dihedral angles alone can effectively regulate sideslip during rapid turns and generate a wide range of equilibrium turn rates while maintaining a constant flight speed and regulating sideslip. We compute the turning performance limitations that arise due to the use of wing dihedral for yaw control, and compare the steady state performance of rigid and flexible-winged aircraft. We present an intuitive but very useful notion, called the effective dihedral, which allows us to extend some of the stability and performance results derived for rigid aircraft to flexible aircraft. In the process, we identify the extent of flexibility needed to induce substantial performance benefits, and conversely the extent to which results derived for rigid aircraft apply to a flexible aircraft. We demonstrate, interestingly enough, that wing flexibility actually causes deterioration in the maximum achievable turn rate when the sideslip is regulated.

PDE Boundary Control of Flexible Aircraft. This AFOSR project also reports on the first PDE control result for controlling flexible wings of MAVs [J4]. Using a simple order of magnitude analysis, we derive conditions under which the wing is structurally statically stable, as well as conditions under which there exists time scale separation between the bending and twisting dynamics. We show that the time scale separation depends on the geometry of the wing cross section, the Poisson's ratio of the wing material, the flight speed and the aspect ratio of the wing. We design independent control laws for bending and twisting. A key contribution of this AFOSR project is the formulation of a partial differential equation (PDE) boundary control problem for wing deformation. PDE-backstepping is used to derive tracking and exponentially stabilizing boundary control laws for wing twist which ensure that a weighted integral of the wing twist (net lift or the rolling moment) tracks the desired time-varying reference input. We show that a control law which only ensures tracking of a weighted integral improves the stability margin of the twisting dynamics sixteen fold. A tracking control law is derived for the wing tip displacement which uses motion planning and a novel two-stage perturbation observer. This work on PDE-based control of wing deformation allows for the use of highly flexible wings on MAVs.

Put together, this AFOSR YIP project provides a comprehensive understanding of the flight dynamics of a robotic aircraft or MAV equipped with articulated wings, and provides a set of con-

trol laws for performing agile maneuvers and for honing the benefits of using highly flexible wings.

This AFOSR project has produced 1 PhD thesis and 1 MS thesis, while 1 PhD thesis is in progress. Also, the PI has published 3 journal papers and 2 pending journal articles. One book chapter article will be published in the AIAA Progress in Aeronautics and Astronautics series.

PhD and MS Theses

- [T1] Aditya Paranjape, Ph.D. in Aerospace Engineering, University of Illinois at Urbana-Champaign, December 2011
Ph.D. Thesis: *Dynamics and Control of Robotic Aircraft with Articulated Wings*
<http://www.ideals.illinois.edu/handle/2142/29818>
- [T2] P. Daniel Kuang, M.S. in Aerospace Engineering, University of Illinois at Urbana-Champaign, December 2011
M.S. Thesis: *Robobat: Dynamics and Control of Flapping Flight Micro Aerial Vehicles*
<http://www.ideals.illinois.edu/handle/2142/29670>

PhD thesis in progress

- [T3] Michael Dorothy, *Mathematical Foundation of Limit-Cycle Based Control of Flapping Flight*

Journal Articles

- [J3] A. A. Paranjape, S.-J. Chung, H. H. Hilton, and A. Chakravarthy, “Dynamics and Performance of a Tailless MAV with Flexible Articulated Wings,” *AIAA Journal*, to appear, 2012.
- [J2] A. A. Paranjape, S.-J. Chung, and M. S. Selig, “Flight Mechanics of a Tailless Articulated Wing Aircraft,” *Bioinspiration & Biomimetics*, vol. 6, 026005, 2011, (20 pp).
- [J1] S.-J. Chung and M. Dorothy, “Neurobiologically Inspired Control of Engineered Flapping Flight,” *Journal of Guidance, Control, and Dynamics*, vol. 33, no. 2, Mar.-Apr. 2010, pp. 440-453. AIAA Infotech Best Paper Award.

Journal Articles under Review or in Preparation

- [J4] A. A. Paranjape, S.-J. Chung, and M. Krstic, “PDE Boundary Control for Flexible Articulated Wings on a Robotic Aircraft,” *IEEE Transactions on Robotics*, under review, 2011.
- [J5] A. A. Paranjape, J. Kim, and S.-J. Chung, “Closed-Loop Perching of Aerial Robots with Articulated Flapping Wings,” to be submitted to *IEEE Transactions on Robotics*, March 2012.

Book Chapter Article

- [B1] M. Dorothy, A. A. Paranjape, P. D. Kuang, and S.-J. Chung, “Towards Bio-inspired Robotic Aircraft: CPG-based Control of Autonomous Flapping and Gliding Flight,” J. Valasek (Ed.), *Intelligent and Autonomous Aerospace Systems, AIAA Progress in Aeronautics and Astronautics Series*, American Institute of Aeronautics and Astronautics (AIAA), Reston, VA, to be published Spring 2012.

Conference Papers

- [C9]] A. Paranjape, J. Kim, N. Gandhi, and S.-J. Chung, “Experimental Demonstration of Perching by an Articulated Wing MAV,” AIAA Guidance, Navigation, and Control Conference, Portland OR, August 2011, AIAA-2011-6403.
- [C8]] A. Paranjape, S.-J. Chung, and M. Krstic, “PDE Boundary Control for Flexible Articulated Aircraft Wings,” AIAA Guidance, Navigation, and Control Conference, Portland OR, August 2011, AIAA-2011-6486.
- [C7]] P. D. Kuang, M. Dorothy, and S.-J. Chung, “RoboBat: Dynamics and Control of a Robotic Bat Flapping Flying Testbed,” AIAA Infotech@Aerospace Conference, St. Louis, MO, Mar. 2011, AIAA-2011-1435.
- [C6]] S.-J. Chung and J.-J. E. Slotine, “On Synchronization of Coupled Hopf-Kuramoto Oscillators with Phase Delays,” invited paper, IEEE Conference on Decision and Control (CDC), Atlanta, GA, Dec. 2010, pp. 3181 - 3187.
- [C5]] A. Paranjape and S.-J. Chung, “Flight Mechanics of a Tailless Articulated Wing Aircraft,” AIAA Atmospheric Flight Mechanics Conference, Toronto, Ontario, invited paper, Aug. 2010, AIAA-2010-7633.
- [C4]] M. Dorothy and S.-J. Chung, “Methodological Remarks on CPG-Based Control of Flapping Flight,” invited paper, AIAA Atmospheric Flight Mechanics Conference, Toronto, Ontario, Aug. 2010, AIAA-2010-7634.
- [C3]] A. Chakravarthy, A. Paranjape, and S.-J. Chung, “Control Law Design for Perching an Agile MAV with Articulated Wings,” AIAA Atmospheric Flight Mechanics Conference, invited paper, Toronto, Ontario, Aug. 2010, AIAA-2010-7934.
- [C2]] A. Paranjape, A. Chakravarthy, S.-J. Chung, and H. H. Hilton, “Performance and Stability of an Agile Tail-less MAV with Flexible Articulated Wings,” AIAA Atmospheric Flight Mechanics Conference, invited paper, Toronto, Ontario, Aug. 2010, AIAA-2010-7937.
- [C1]] S.-J. Chung, J. Stoner, and M. Dorothy, “Neurobiologically Inspired Control of Engineered Flapping Flight,” AIAA Infotech@Aerospace and Unmanned Unlimited Conference and Exhibit, Best Paper Award, Seattle, WA, 6-9 April 2009, AIAA-2009-1929.

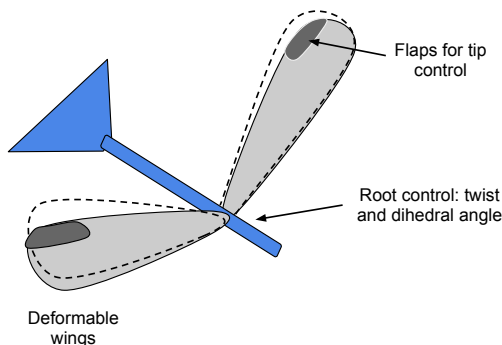
1 Introduction

There is a considerable interest in developing robotic aircraft inspired by birds and bats [44, 14, 31] and insects [24, 22, 21, 107]. In contrast with insects whose wings are well modeled as simple

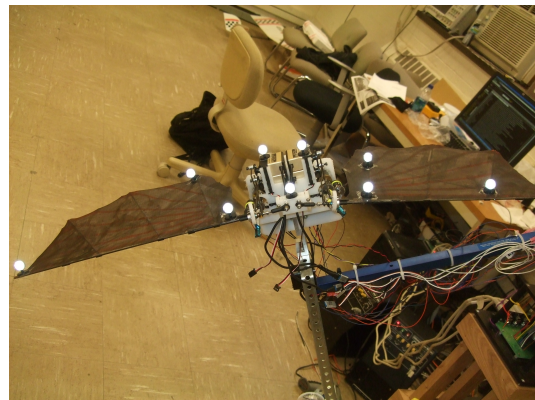
rigid wings, both wing flexibility and wing articulation are believed to play a key role in flight performance and agility for bird and bat flight [90]. The broader goal is to learn and mimic avian flight with the ultimate objective of designing unmanned aerial vehicles which are autonomous, agile and capable of flying in constrained environments [57]. Birds are natural role models for designing robotic micro air vehicles (MAVs) wherein the aforementioned attributes can be engineered. MAVs typically fly in a low Reynolds number range of $10^3 - 10^5$ [54] which coincides with that of the birds. Therefore, it is worth investigating the mechanics of avian flight and making an attempt to reverse-engineer them. Conversely, a study of the flight mechanics of MAVs can shed light on several aspects of bird flight.

Birds lack a vertical tail. Instead, the wing dihedral and incidence angles are controlled actively as birds execute agile and even spatially constrained maneuvers. Birds are known to have a very complex wing structure, with a wide range of “actuators.” The wings can flap, twist and change the sweep angle on demand. They have a wide range of feathers which serve as flaps and spoilers. The hair on bird wings can sense local flow conditions, and feedback from these sensors is sent to the feathers which are, either passively or actively, oriented to optimize the flow conditions on the wing for stability and maneuverability.

Over-actuation to the extent seen in birds is difficult to engineer in aircraft because of well understood considerations such as weight penalty, actuator limitations, sensor design, etc. Therefore, it is necessary to abstract out the underlying phenomena and understand their implications for stability and control. That way, they can be engineered onto actual aircraft. This is the motivation behind this AFOSR project.



(a) Robotic aircraft concept



(b) Robotic bat at UIUC

Figure 1: Figure (a) shows a robotic aircraft with flexible wings controlled at the wing root (by servo actuators) and the tip (by flaps). Figure (b) shows a robotic bat testbed where the control laws proposed in this project can be tested [44, 14].

This AFOSR project contributes to the broader problem of developing a flapping MAV capable of agile flight in constrained environments, such as the conceptual MAV in Fig. 1(a). Chung and Dorothy [14] studied a neurobiologically-inspired controller for flapping flight, and demonstrated it on a robotic testbed shown in Fig. 1(b). Their controller could switch in a stable and smooth fashion between flapping and gliding flight. Gliding is essential during soaring, landing and perching (see

Fig. 2 for a schematic diagram of a perching maneuver). This project aims to provide the analytical foundations for using wing articulation to perform agile maneuvers while gliding and landing.

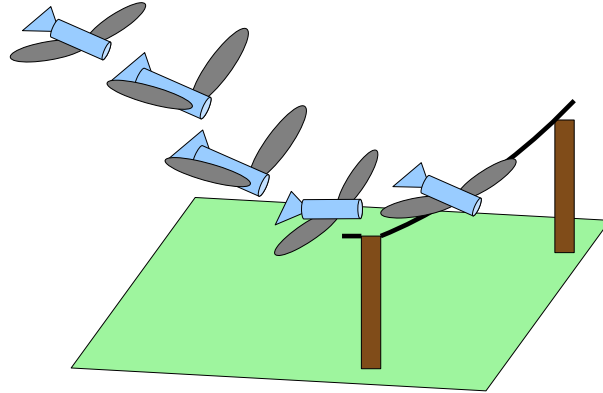


Figure 2: Schematic of a perching maneuver executed by a tailless articulated wing aircraft.

Like any problem in flight mechanics and control, this project approaches the chosen problem along three directions: performance, stability and control. Each facet has been addressed in the report:

- Performance: we focus on steady state performance metrics such as the turn rate, gliding angle and speed. Turn rate is of particular interest because this performance metric would be most affected by the absence of a vertical tail. We also analyse the influence of wing flexibility on the performance metrics.
- Stability: we use bifurcation analysis to study the nature of stability of the turn and wings level equilibria. We derive literal approximations to some lateral stability indicators.
- Control: we demonstrate control and control-related issues through a combination of theoretical analysis and experiments on an actual MAV. We also design PDE-based control schemes to control the deformation of a flexible wing. The control design process makes use of several features of MAV geometry and flight regime.

One point that is particularly worth highlighting is the restriction of our analysis to MAVs. This restriction comes about due to the fact that wing articulation proposed in this project would be impractical for larger aircraft. The low flight speed and small size of MAVs lead to several interesting consequences. The low flight speeds imply that the local angle of attack distribution on the wing is a nonlinear function of the angular velocity of the aircraft. The nonlinearity manifests itself in, for example, the peculiar relation between the turn rate and the commanded dihedral as described later in the report. The low flight speed and the Young's modulus together lead to time scale separation between the twisting and bending dynamics of a flexible wing, which simplifies the control design process significantly in practical situations.

The problems that we have considered in the AFOSR project have several novel elements. Before stating the contributions of the project, we briefly discuss the state of the art.

2 Literature Review

Fixed and flapping wing MAVs have been extensively studied in the literature. The reader is referred to an excellent compendium of papers [54] which showcases some of the work done in this area until circa 2000. The idea of using cant-angle winglets for control was investigated experimentally by Bourdin, Gatto and Friswell [8, 28] for larger aircraft operating at high Reynolds numbers. However, their analysis was restricted to calculating the aerodynamic moments arising from the use of cant-angle winglets. Wickenheiser and Garcia [105, 106] studied the dynamics of morphing aircraft and demonstrated perching using, among other forms of articulation, variable wing incidence. Reich *et al.* [76] experimentally studied the aerodynamic performance of a wing of variable incidence for perching. Crowther [18] showed that a perched landing can be achieved using a simple pitch-up maneuver, and a similar conclusion was obtained after optimization by Cory and Tedrake [17].

Stenfelt and Ringertz [92, 93] studied the stability and control of tailless aircraft equipped with a split flap mechanism. Shtessel, Buffington and Banda [86] designed a sliding mode-based controller for tailless fighter aircraft, while Patel and co-authors [66] designed a robust adaptive controller for tailless aircraft in the presence of actuator failures. Recently, Obradovic and Subbarao [56] investigated the power requirement for morphing, and used it as a basis to compare wing morphing and the traditional aileron-based control in different flight regimes. The lateral stability and control of birds, and in particular, the role of wing dihedral, have been studied extensively by Sachs and co-authors [81, 79, 80]. Sachs has demonstrated that for air vehicles whose size and speed (and hence, the Reynolds number) are similar to those of birds, wings are sufficient to provide lateral stability thereby reducing, if not eliminating altogether, the need for a vertical tail. Tran and Lind [99] numerically computed the stability of an aircraft equipped with variable symmetric dihedral and incidence. Their wing model consisted of an assemblage of rigid segments.

A variety of aircraft models incorporating wing and fuselage flexibility have been proposed in the literature, although most of these models do not consider wing articulation. Waszak and Schmidt [104] derived a complete nonlinear model of an aircraft with flexible wings. Their aerodynamic model, however, assumed a steady flow, and their frame of reference consisted of the so-called *mean axes* which are hard to locate in a practical situation. Tuzcu and Meirovitch [52] extended their model in several ways: they used a more intuitive reference frame (the conventional body axes) and a more accurate Theodorsen's unsteady aerodynamics theory for computing the forces and moments [97]. Recently, Nguyen and Tuzcu [55] presented a dynamic model for a fully flexible aircraft. These papers worked with a small-strain, small-displacement beam theory. In contrast, Patil and co-authors [67, 71] derived a geometrically exact (large displacement) small-strain nonlinear beam model, and used it to study the dynamics and stability of flying wings. Shearer and Cesnik [85] and Su and Cesnik [96] used nonlinear flight dynamic and structural models to investigate the effects of structural nonlinearities on the dynamic stability of aircraft characterized by large aspect ratio wings and blended wing-body configurations, respectively. Baghdadi and co-authors [3] used bifurcation analysis to study the performance and stability of a flexible aircraft model based on Ref. [104] and concluded that flexibility must be accounted for carefully during the control design process. They also demonstrated that a control law designed assuming a rigid configuration could trigger instabilities in an otherwise identical aircraft with flexible wings. Rodden [77] derived analytical expressions, backed by experimental approximations, for increments in the rolling moment derivatives arising from aeroelastic effects.

It has been demonstrated in the literature that aeroelastic instabilities such as wing divergence

and flutter can be mitigated using flap-based effectors [5, 74] or passive energy sinks (for flutter) [36]. There is a substantial amount of literature on boundary control theory of PDEs (see Refs. [78, 43, 42, 12, 13, 47] for material pertinent to this report and the references cited therein). There are two sets of methods for boundary control of PDEs. The first set consists of methods that seek to convert the PDEs into ordinary differential equations using approximation methods such as those of Galerkin or Rayleigh-Ritz [13, 34], or using operator theory [19, 9]. The second set consists of methods that keep the PDEs intact, and use a “model-following” approach as described in a recent book by Krstic and Smyshlyaev [42].

If a PDE is approximated by Galerkin’s method, or converted into an ODE form using operator theory, the problem of achieving an integral objective reduces to a standard output control problem. Whereas solutions to output control problems in an ODE setting are abundantly known, an ODE-based approximation to PDEs usually leads to systems having large orders. The ODE-based control design process usually becomes tedious, the control laws become non-intuitive, and the tracking errors could be large for a class of inputs when a poor choice is made for the basis functions which capture the time-varying boundary conditions. Ref. [12] also points out that a finite-state approximation may wrongly render fundamental system theoretic properties like controllability and observability to be functions of the approximation. Stability analysis based on finite state approximation is vulnerable to spillover instabilities which arise due to inadequate accounting of the residual modes [4, 51].

On the other hand, keeping PDEs intact makes the control law design more intuitive. It has been used in the past for maneuvering robotic arms [70, 42], controlling the Navier-Stokes model [102] and suppressing vibrations in a flexible beam [32]. A gain-scheduling based approach for nonlinear PDEs has been presented in Ref. [88], while Krstic and Smyshlyaev [43] derived an adaptive controller for parabolic PDEs.

3 Main Contributions

3.1 Performance and Stability

As we stated earlier, this AFOSR project is dedicated to MAVs whose speed and size present several distinct characteristics from the point of view of control and stability. The small size of MAV wings makes wing articulation practically feasible. Unlike conventional fixed wing aircraft, an articulated wing aircraft changes its configuration routinely and, therefore, stability is closely tied to the nature of the maneuver being executed. We use bifurcation analysis [30, 48, 65] to explore the dynamics of tailless aircraft equipped with articulated wings. Bifurcation analysis not only measures the stability characteristics of the aircraft, but also helps predict the performance limitations that arise because of the use of asymmetric dihedral. We study a rigid aircraft model to gain a foothold, and then perform a similar analysis on an aircraft with flexible wings for comparison.

The report includes detailed theoretical and linear computational analyses of the lateral dynamics. Longitudinal dynamics are not affected by the absence of a vertical stabilizer. Analytical expressions for lateral-directional aerodynamic force and moment derivatives offer valuable insight into the maneuver-dependence of stability and help identify the source of lateral-directional instability, which is subsequently verified computationally. The analytical expressions also help identify potentially dangerous situations where the control effectiveness of the dihedral may switch sign in the midst of certain maneuvers.

It is known that the wing dihedral angle can be varied to perform slow, steep descents [81, 98]. We compute the gliding flight equilibria numerically along with their stability to identify bounds on longitudinal performance. A knowledge of the longitudinal trims can help formulate landing and perching strategies in spatially-constrained environments without resorting to maneuvers like spin [75] and aid the design of control laws for perching [10].

Next, we compare select performance metrics and stability of the rigid MAV with those of a similar MAV equipped with flexible wings. The purpose of this analysis is two-fold. First, it helps to identify the benefits and limitations of using wing flexibility. Second, and less obviously, it helps to identify the extent to which a rigid MAV model can accurately capture the dynamics of a flexible wing MAV. The flight dynamics will be rendered unstable if the wing is structurally unstable. On the other hand, if the structural stability of the wing can be guaranteed, then the performance and stability of the motion can be computed reliably by considering “macroscopic” parameters like the resultant forces which depend on the shape, rather than stability, of the wing. Therefore, an analysis like the one in this project would depend largely on the wing geometry (which is usually well known *a priori*) rather than a precise knowledge of the elastic parameters.

The specific questions answered for a flexible-winged MAV include:

1. For the wing of a typical bird-sized MAV, what value of Young’s modulus (E) should the wing have in order for the MAV to offer a significant performance improvement over a rigid wing MAV? Equivalently, until what point is the open loop analysis of a rigid aircraft relevant to a flexible-winged aircraft? The notion of effective dihedral is introduced in a bid to answer these questions.
2. A stiff wing may be required for certain maneuvers. Axial tension in the wing is an intuitive stiffener. How effective and useful is it? We answer this question in the negative - it is effective, but of limited utility.
3. How is the stability of the motion altered in the presence of flexible wings? The wings are assumed to be quasi-statically deformed and, therefore, the structural dynamics of the wings have no bearing on the conclusion. In other words, the wing is assumed to be structurally stable and its dynamics sufficiently faster than the aircraft.
4. Is there a measurable improvement in the steady state turning performance? Steady state turn rate is the only agility metric which is based entirely on a steady maneuver [61]. It is also an important benchmark to evaluate the efficacy of a yaw control mechanism.

3.2 Control

The ideas discussed above were subjected to experimental validation involving open loop as well as closed loop flight tests. The purpose of the experiments is to demonstrate (a) the effectiveness of symmetric dihedral for flight path angle control, (b) yaw control using asymmetric dihedral, and (c) some elements of a perching maneuver [26].

One of the key contributions of this AFOSR project is a boundary control problem for wing twist which could be extended to a wider class of hyperbolic partial differential equations (PDEs). We also consider motion planning for the bending dynamics of an Euler-Bernoulli beam using a novel estimator-based scheme. The problem of controlling a flexible wing presents unique problems as well as helpful features. A flexible wing represents a coupled twist-bending problem in the simplest

case, and a coupled twist-bending-rigid-motion problem in the most general case. Either way, problems with coupled PDEs are difficult to solve because the only unified approach to assembling a system of diverse PDEs requires that they be converted into an equivalent or approximate ODE system. This is a cumbersome route.

We show that the twisting dynamics of the MAV wing are faster than the bending dynamics, and the time scale separation depends on the aspect ratio of the wing. We design independent tracking controllers for twist and bending, which can be applied effectively to control the coupled twist-bending dynamics. We also identify the extent of flexibility required to trigger a structural instability in an MAV at routine flight speeds.

We show that wing twist can be stabilized rapidly using a root-based actuator driven by a PDE backstepping controller. The procedure is called backstepping because it involves a Volterra operator with a lower triangular structure similar to backstepping transforms for ordinary differential equations [41, 42]. It is a continuum analogue of the backstepping transformations in ODEs and allows the controller acting at the boundary to compensate for the undesired (unmatched) dynamics. We also design a tracking control (which is considerably harder when the actuator is located only at the boundary) based on motion-planning which can be added on top of the backstepping controller.

For a class of input-output combinations, we show that the twist dynamics have a finite relative degree which permits a more traditional approach to control design. We show that the tracking controller renders the cantilever wing into the form of a clamped-clamped beam, which improves the stability margin of the twist dynamics by a factor of sixteen. An adaptive controller for a limited class of parametric uncertainties is also derived for tip-based actuators in general, and root-based actuators when the output is the rolling moment.

There are several controller designs in the literature for stabilizing and controlling beam bending (see, for example, [32, 88, 101, 27, 40]). We design a perturbation observer-based controller to facilitate a motion planning-based tracking controller for bending. The output of interest is the displacement of the wing tip. As the name suggests, the perturbation observer designed here uses adaptation to estimate the external forces acting on the system. The observer is split into a “particular” and a “homogeneous” component (the notions are made more precise later). Since the homogeneous component is stable and not driven directly by external feedback, it is simpler to design a control law for it. The same control signal is sent to the actual system, whose states then converge exponentially rapidly to a bounded envelope around the observer states.

4 Biologically Inspired CPG-Based Control

The flapping motion in bats combines many different joints and muscles to create rhythmic motions which produce the aerodynamic forces required to sustain flight. With the current state of the actuator/structure technology, we are unable to mimic the strength and flexibility of the distributed structure of bones, joints and ligaments. More specifically, we are unable to produce muscle-strength actuation of the entire system using mechanical actuators. For this purpose, we have settled on starting our investigation with three main modes of motion: flapping, twisting, and lead-lag (sometimes referred to as plunging, pitching, and sweeping). These three motions (shown in Figure 3) have the strongest connection to traditional flight models and were the first to be discussed in observations of animal flight [2]. Azuma also notices that the phase differences between the motions is extremely important [2]. Next we consider how to use CPGs for precise control of

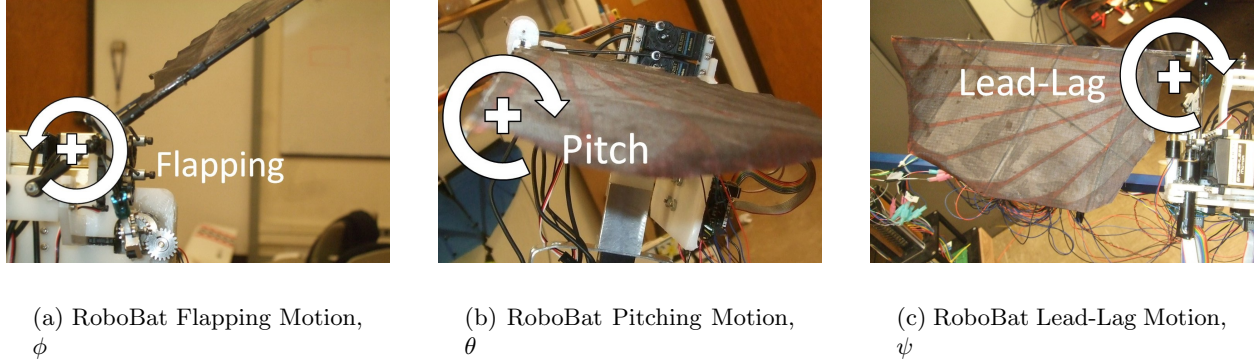


Figure 3: Main wing motions used by RoboBat

phase differences between the three motions.

4.1 Central Pattern Generators

Many creatures produce their motion by synchronizing periodic motions of limbs, such as running, swimming or flapping. They do this by coupling biological oscillators and synchronizing their outputs. Biological oscillators rely on short timescale (ms) neuron dynamics including spike-bursting, spike frequency adaptation, and post-inhibitory rebound. Herrero-Carrón, et. al. [33] designed a control law for modular robots by approximating short timescale neuron dynamics. Because there is such a short timescale required for integration, the neuron dynamics were integrated offline. We are unlikely to be able to perform such strict mimicry in an online controller as we add additional neurons for feedback, active control of phase differences, or gait transitions.

In order to make online control more feasible, we can emulate these biological oscillators by using coupled nonlinear limit cycle oscillators. A limit cycle oscillator converges to a stable trajectory which is called the limit cycle. Because of this convergence the oscillator will quickly forget sporadic disturbances and converge back to the stable limit cycle. If the oscillator itself is a smooth vector field, we can smoothly transition between desired trajectories without abrupt changes being required in the motor output.

This type of control design allows the complicated synchronization and trajectory computations to be performed according to simple rules that provide the desired oscillatory behavior. If we can then influence body motion by simply tuning top-level inputs into the CPG network, we can achieve the dimension reduction that allows the control problem to be computationally feasible. Vertebrate brains send top-level chemical signals which modulate, start, and stop CPG behavior, but do not micromanage the joint trajectories [91].

Following our previous work [14], we use the following limit-cycle model called the Hopf oscillator, named after the supercritical Hopf bifurcation model with $\sigma = 1$:

$$\dot{\mathbf{x}} = \mathbf{f}(\mathbf{x}; \rho; \sigma) + \mathbf{u}(t) \quad \text{with } \mathbf{x} = (u - a, v)^T \quad \text{and} \quad (1)$$

$$\mathbf{f}(\mathbf{x}; \rho; \sigma) = \begin{bmatrix} -\lambda \left(\frac{(u-a)^2 + v^2}{\rho^2} - \sigma \right) & -\omega(t) \\ \omega(t) & -\lambda \left(\frac{(u-a)^2 + v^2}{\rho^2} - \sigma \right) \end{bmatrix} \mathbf{x}$$

where the $\lambda > 0$ denotes the convergence rate to the symmetric limit circle of the radius $\rho > 0$

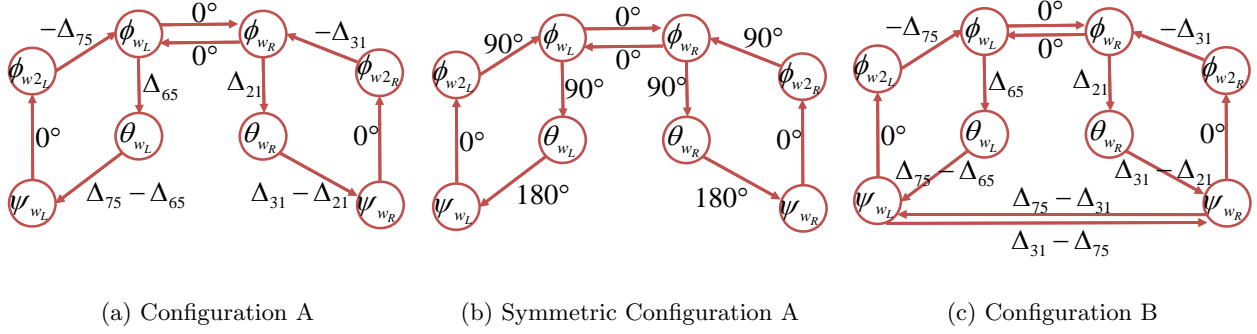


Figure 4: Example graph configurations of the coupled Hopf oscillators on balanced graphs.

and $\mathbf{u}(t)$ is an external or coupling input. The bifurcation parameter σ can change to a negative number (e.g. -1 such that $\left(\frac{(u-a)^2+v^2}{\rho^2} + 1\right)$). This would change the stable limit cycle dynamics to the dynamics with a globally stable equilibrium point at the bias “ a ” [95]. Such a change can be used to turn the flapping oscillatory motion to the gliding mode, as was seen in [14]. This could be used to mimic many animal flight strategies. Later sections of this paper discuss terminal perching control, assumed to be in a gliding phase. Often, bats and birds will transition to gliding in order to shed energy well before an actual perching maneuver is performed. In [14], it was shown that coupled networks of Hopf oscillators on balanced graphs exhibit smooth exponentially stable behavior in both oscillatory mode and fixed point mode.

The possibly time-varying parameter $\omega(t) > 0$ determines the oscillation frequency of the limit cycle. A time-varying $a(t)$ sets the bias to the limit cycle such that it converges to $u(t) = \rho \cos(\omega t + \delta) + a$ and $v(t) = \rho \sin(\omega t + \delta)$ on a circle. The output variable to generate the desired oscillatory motion of each joint is the first state u from the Hopf oscillator model in Eq. (1).

Phase synchronization means an exact match of the scaled amplitude or the frequency in this paper. Hence, phase synchronization permits different actuators to oscillate at the same frequency but with a prescribed phase lag. In essence, each CPG dynamic model in Eq. (1) is responsible for generating the limiting oscillatory behavior of a corresponding joint, and the diffusive coupling among CPGs reinforces phase synchronization. For example, the flapping angle has roughly a 90-degree phase difference with the pitching joint to maintain the positive angle of attack (see the actual data from birds in [2]). The oscillators are connected through diffusive couplings, and the i -th Hopf oscillator can be rewritten with a diffusive coupling with the phase-rotated neighbor.

$$\dot{\mathbf{x}}_i = \mathbf{f}(\mathbf{x}_i; \rho_i) - k \sum_{j \in \mathcal{N}_i}^{m_i} \left(\mathbf{x}_i - \frac{\rho_i}{\rho_j} \mathbf{R}(\Delta_{ij}) \mathbf{x}_j \right) \quad (2)$$

where the Hopf oscillator dynamics $\mathbf{f}(\mathbf{x}_i; \rho_i)$ with $\sigma = 1$ is defined in Eq. (1), \mathcal{N}_i denotes the set that contains only the local neighbors of the i -th Hopf oscillator, and m_i is the number of the neighbors. The 2×2 matrix $\mathbf{R}(\Delta_{ij})$ is a 2-D rotational transformation of the phase difference Δ_{ij} between the i -th and j -th oscillators. The positive (or negative) Δ_{ij} indicates how much phase the i -th member leads (or lags) from the j -th member and $\Delta_{ij} = -\Delta_{ji}$. The positive scalar k denotes the coupling gain.

Numerous configurations are possible as long as they are on balanced graphs [16] and we can

choose either a bidirectional or a uni-directional coupling between the oscillators. The numbers next to the arrows in Fig. 4 indicate the phase shift Δ_{ij} , hence $\Delta_{ij} > 0$ indicates how much phase the i -th member leads. Figure 4(a) shows the choice of coupling used in this paper, where ϕ_w , θ_w , and ψ_w are flapping angle, twist angle, and lead-lag angle, respectively. Subscripts L and R refer to left and right wings. The graph is balanced. Further, all the phase shifts (Δ_{ij}) along one cycle add up to a modulo of 2π . The proof of stability of (2) is given in [14]. As mentioned in [25], this type of oscillator generalizes other types of waveform control such as the split-cycle [23].

4.2 Control Design from Physical Intuition and Biological Observation

Our previous work [14] provided a simple intuition for phase difference control of longitudinal motion in flapping flight. With a zero bias lead-lag and a center of gravity coinciding with the stroke plane, a phase difference of 270 deg between the flapping CPG and the lead-lag CPG gives Azuma’s [2] elliptical model of flapping: negative lead-lag on downstroke, positive lead-lag on upstroke. The simplest analysis combines a maximum force with the most-negative lead-lag at the middle of the downstroke to predict a pitch-down moment on the body. Alternatively, if we see the phase difference to 90 deg, we see the maximum force coinciding with the maximum positive lead-lag at the middle of the downstroke, predicting a pitch-up moment. This intuition has been confirmed in numerical simulations and open loop experiments on the RoboBat[14, 15, 44].

5 Equations of Motion for an Articulated Wing Aircraft

The dynamic model derived in this chapter is general enough that it can be applied to a wider class of problems such as flapping and a complete aeroelastic analysis of aircraft. This chapter consists of two sections. The equations of motion for a flexible aircraft are derived in the first section, and specialized to a rigid aircraft in the second section.

5.1 Notation

Capital letters are reserved for forces, matrices, and for denoting coordinate frames. Small letters are used for scalars when not in bold, and for vectors when used with bold font. Given a vector $\mathbf{x} \in \mathbb{R}^3$, $S(\mathbf{x})$ denotes the cross product operator, i.e.; for any two vectors \mathbf{x} , $\mathbf{y} \in \mathbb{R}^3$, $S(\mathbf{x})\mathbf{y} \triangleq \mathbf{x} \times \mathbf{y}$. Similarly, $S^2(\mathbf{x})\mathbf{y} = S(\mathbf{x})(S(\mathbf{x})\mathbf{y}) = \mathbf{x} \times (\mathbf{x} \times \mathbf{y})$. Given a variable $p(t, y)$, its time derivative is denoted by $\dot{p}(t, y) \triangleq \frac{\partial p(t, y)}{\partial t}$. Its spatial derivative is denoted by $p'(t, y) \triangleq \frac{\partial p(t, y)}{\partial y}$. Note that when $p(t, y) \equiv p(t)$, $\dot{p}(t) = \frac{dp(t)}{dt}$.

5.2 Coordinate Frames of Reference

Given frames F and G , the matrix \mathbf{T}_{FG} is a rotation matrix which transforms the components of a vector from the G frame to F . The body frame, denoted by B , is attached to the body with the $x - z$ plane coincident with the aircraft plane of symmetry when the wings are undeflected. The x axis points towards the aircraft nose. The z axis points downwards, and the y is defined to create a right handed coordinate system. The coordinate frames have been illustrated in Fig 5, together with the dimensions of the aircraft considered for numerical analysis.

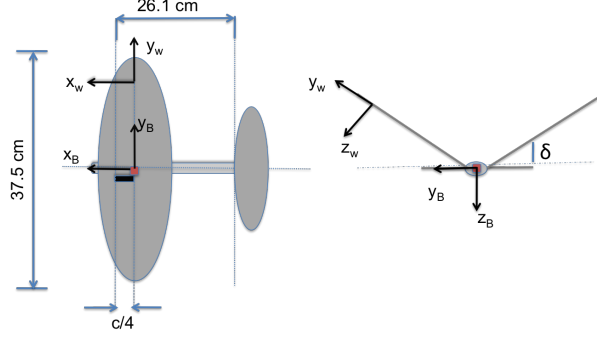


Figure 5: A schematic of the aircraft showing the dimensions and the coordinate systems used to model the aircraft.

Consider the frame R based at the right wing root. Its origin coincides with that of the B frame, which is akin to neglecting the fuselage width. This assumption does not alter the rotation matrices in any way. The frame R is related to the B frame via three rotations at the wing root: a sweep rotation β_R about the z -axis, followed by a dihedral rotation δ_R about the $-x$ -axis, and a rotation θ_R about the y axis. The y axis points along the wing elastic axis. Thus,

$$\mathbf{T}_{BR} = \begin{bmatrix} \cos \beta_R & -\sin \beta_R & 0 \\ \sin \beta_R & \cos \beta_R & 0 \\ 0 & 0 & 1 \end{bmatrix} \begin{bmatrix} 1 & 0 & 0 \\ 0 & \cos \delta_R & \sin \delta_R \\ 0 & -\sin \delta_R & \cos \delta_R \end{bmatrix} \begin{bmatrix} \cos \theta_R & 0 & \sin \theta_R \\ 0 & 1 & 0 \\ -\sin \theta_R & 0 & \cos \theta_R \end{bmatrix} \quad (3)$$

A similar matrix can be defined for the left wing. The matrix \mathbf{T}_{BR} is introduced here in the most general form, i.e., no rotation is ignored, which makes it applicable to flapping flight dynamics. From hereon, we assume that $\beta_R = \beta_L = 0$.

The frame $S \equiv S(y)$ is the frame located at a spanwise wing station with origin at the elastic center, and y axis pointing along the elastic axis. The frame S is related to R via two rotations: a rotation about the x axis through the strain $\xi'(y)$, and a rotation (twist) $\theta_s(y)$ about the y axis. Thus,

$$\mathbf{T}_{RS} = \begin{bmatrix} \cos \theta_s(y) & 0 & \sin \theta_s(y) \\ \sin(\xi'(y)) \sin \theta_s(y) & \cos(\xi'(y)) & -\sin(\xi'(y)) \cos \theta_s(y) \\ -\cos(\xi'(y)) \sin \theta_s(y) & \sin(\xi'(y)) & \cos(\xi'(y)) \cos \theta_s(y) \end{bmatrix} \quad (4)$$

In the interests of analytical tractability, for the purposes of computing the velocities and acceleration terms, it will be assumed that $\mathbf{T}_{BS} = \mathbf{T}_{BR}$, i.e., the deformations are small enough that they do not alter the coordinate transformations. However, in Sec. 5.7, this assumption is relaxed for computing the aerodynamic forces and moments. This is the primary source of the difference in the forces and moments produced by rigid and flexible wings.

5.3 Calculating the Velocity at a Spanwise Station

The angular velocity of the right wing, $\boldsymbol{\omega}_R$ with components in the body frame, is given by

$$\boldsymbol{\omega}_R = \begin{bmatrix} -\cos \beta_R & -\cos \delta_R \sin \beta_R & 0 \\ -\sin \beta_R & \cos \delta_R \cos \beta_R & 0 \\ 0 & \sin \delta_R & 1 \end{bmatrix} \begin{bmatrix} \dot{\delta}_R \\ \dot{\theta}_R \\ \dot{\beta}_R \end{bmatrix} \quad (5)$$

It is calculated using a 3-1-2 Euler angle sequence which is also used to calculate \mathbf{T}_{BR} . The same sequence can be used to model a flapping wing, in which case, the amplitude and phase of the motion corresponding to each degree of freedom needs to be prescribed. In contrast, most flapping wing models prefer to identify a stroke plane in which the flapping motion is constrained, and which also contains the twist axis (see Refs. [14, 7, 87] and the references cited therein).

Let $\mathbf{y} = [0 \ y \ \xi]^T$ denote the coordinates of a spanwise station on the wing along the twisting axis. Then the local wind velocity, with components in the local station frame, is given by

$$\mathbf{V} = \mathbf{T}_{SB}\mathbf{u}_B + \mathbf{u}_f + \mathbf{T}_{SB}S(\boldsymbol{\omega}_B + \boldsymbol{\omega}_R)\mathbf{T}_{BR}\mathbf{y} \quad (6)$$

A similar expression can be determined for the angular velocity of the left wing at the root, $\boldsymbol{\omega}_L$, and the local velocity at a spanwise station on the left wing.

The aerodynamic center is assumed to be located at the quarter chord point. The velocity at the 3/4-chord point of a spanwise station is used for calculating the angle of attack, and it is given by

$$\mathbf{V}_{3/4}(y) = \mathbf{V} + S(\boldsymbol{\omega}_s)\mathbf{x}_{3/4} \quad (7)$$

where $\mathbf{x}_{3/4} = [(x_a - 0.5)c \ 0 \ 0]^T$. Let $[u_{3/4}(y), v_{3/4}(y), w_{3/4}(y)]$ denote the components of $\mathbf{V}_{3/4}$ in the local station frame, and $V_{3/4}$ its magnitude. Then, the local angle of attack and sideslip can be calculated using

$$\tan \alpha(y) = \frac{w_{3/4}}{u_{3/4}}, \quad \sin \beta(y) = \frac{v_{3/4}}{V_{3/4}} \quad (8)$$

5.4 Equations of Motion of the Aircraft

Let m_R and m_L denote the masses of the right wing and left wing, respectively. Let \tilde{m}_R and \tilde{m}_L denote the masses per unit length of the right wing and left wing, respectively. Let m denote the total mass of the aircraft, and let \mathbf{r}_{CG} denote the position of its center of gravity. Let $\mathbf{r}_s = [x_e c, 0, 0]^T$ denote location of the center of gravity with respect to the wing twist, and let $\mathbf{y} = [x_e c \cos \theta_s(y), y, \xi - x_e c \sin \theta_s(y)]^T$ denote the position of the center of gravity of a wing station in the wing root frame. Let $\boldsymbol{\omega}_s \triangleq [0 \ \dot{\theta}_s \ 0]^T$ denote the angular velocity of a given wing station due to twisting.

The translational equations of motion are given by

$$\begin{aligned}
& m (\dot{\mathbf{u}}_B + S(\boldsymbol{\omega}_B)\mathbf{u}_B + S(\dot{\boldsymbol{\omega}}_B)\mathbf{r}_{CG} + S^2(\boldsymbol{\omega}_B)\mathbf{r}_{CG} + S(\boldsymbol{\omega}_B)\dot{\mathbf{r}}_{CG}) + \\
& \tilde{m}_R \int_0^{b/2} ((S(\boldsymbol{\omega}_R + \boldsymbol{\omega}_B)S(\boldsymbol{\omega}_R) + S(\dot{\boldsymbol{\omega}}_R))\mathbf{T}_{BR}\mathbf{y} + S(\boldsymbol{\omega}_R)\mathbf{T}_{BR}\mathbf{u}_f) dy \\
& + \tilde{m}_L \int_{-b/2}^0 ((S(\boldsymbol{\omega}_L + \boldsymbol{\omega}_B)S(\boldsymbol{\omega}_L) + S(\dot{\boldsymbol{\omega}}_L))\mathbf{T}_{BR}\mathbf{y} + S(\boldsymbol{\omega}_L)\mathbf{T}_{BR}\mathbf{u}_f) dy \\
& + \tilde{m}_R \int_0^{b/2} (\mathbf{T}_{BR}\dot{\mathbf{u}}_f(y) + S(\boldsymbol{\omega}_B + \boldsymbol{\omega}_R + \mathbf{T}_{BR}\boldsymbol{\omega}_s)\mathbf{T}_{BR}(\mathbf{u}_f + S(\boldsymbol{\omega}_s)\mathbf{r}_s) + \mathbf{T}_{BR}S(\dot{\boldsymbol{\omega}}_s)\mathbf{r}_s) dy \\
& + \tilde{m}_L \int_{-b/2}^0 (\mathbf{T}_{BR}\dot{\mathbf{u}}_f(y) + S(\boldsymbol{\omega}_B + \boldsymbol{\omega}_L + \mathbf{T}_{BR}\boldsymbol{\omega}_s)\mathbf{T}_{BR}(\mathbf{u}_f + S(\boldsymbol{\omega}_s)\mathbf{r}_s) + \mathbf{T}_{BR}(S(\dot{\boldsymbol{\omega}}_s)\mathbf{r}_s)) dy = [X_B \ Y_B \ Z_B]^T
\end{aligned} \tag{9}$$

where $[X_B, Y_B, Z_B]$ is the net force acting on the aircraft (aerodynamic plus gravitational), with components in the body frame. An expression for the net force is given Sec. 5.7. The position vector of the center of gravity (CG) is given by

$$\dot{\mathbf{r}}_{CG} = \frac{1}{m} \left(\tilde{m}_R \int_0^{b/2} (\mathbf{u}_f + S(\boldsymbol{\omega}_R)\mathbf{T}_{BR}\mathbf{y}) dy + \tilde{m}_L \int_{-b/2}^0 (\mathbf{u}_f + S(\boldsymbol{\omega}_L)\mathbf{T}_{BR}\mathbf{y}) dy \right) \tag{10}$$

For highly flexible or rapidly flapping wings, the dynamics of the CG serve to couple the translational and rotational dynamics tightly. The CG location can be changed using an actuated mass, such as the bob weight in Doman, Oppenheimer, and Sigthorsson [23], for controlling the aircraft attitude.

The moment of inertia of the right wing is given by

$$\mathbf{J}_R = - \int_0^{b/2} S^2(\mathbf{T}_{BR}\mathbf{y} + \mathbf{T}_{BR}\mathbf{x}) dm \tag{11}$$

and \mathbf{J}_L is defined similarly. Let $\rho_{w,R}$ and $\rho_{w,L}$ denote the densities of the right and left wing, respectively, and \mathbf{J} is the total moment of inertia of the aircraft. It has been assumed that the moment of inertia of the wing is constant in magnitude, i.e., the effect of wing bending and twist on the net moment of inertia of the aircraft is ignored. Subject to this assumption, the following dynamic equation for rotational motion is obtained:

$$\begin{aligned}
& \mathbf{J}\dot{\boldsymbol{\omega}}_B + S(\boldsymbol{\omega}_B)\mathbf{J}\boldsymbol{\omega}_B + mS(\boldsymbol{\omega}_B)S(\mathbf{r}_{CG})\mathbf{u}_B + mS(\mathbf{r}_{CG})\dot{\mathbf{u}}_B + S(\dot{\mathbf{r}}_{CG})\mathbf{u}_B + \mathbf{J}_R\dot{\boldsymbol{\omega}}_R + \mathbf{J}_L\dot{\boldsymbol{\omega}}_L \\
& + S(\boldsymbol{\omega}_B)(\mathbf{J}_R\boldsymbol{\omega}_R + \mathbf{J}_L\boldsymbol{\omega}_L) + (S(\boldsymbol{\omega}_R)\mathbf{J}_R - \mathbf{J}_R S(\boldsymbol{\omega}_R))(\boldsymbol{\omega}_B + \boldsymbol{\omega}_R) + (S(\boldsymbol{\omega}_L)\mathbf{J}_L - \mathbf{J}_L S(\boldsymbol{\omega}_L))(\boldsymbol{\omega}_B + \boldsymbol{\omega}_L) \\
& - \tilde{m}_R \int_0^{b/2} \left(S(\boldsymbol{\omega}_B + \boldsymbol{\omega}_R)S(\mathbf{T}_{BR}\mathbf{y})\mathbf{T}_{BR}(\mathbf{u}_f + S(\mathbf{r}_s)\boldsymbol{\omega}_s) + S(\mathbf{T}_{BR}\mathbf{y})\mathbf{T}_{BR}(\dot{\mathbf{u}}_f + S(\mathbf{r}_s)\dot{\boldsymbol{\omega}}_s) \right) dy \\
& - \tilde{m}_L \int_{-b/2}^0 \left(S(\boldsymbol{\omega}_B + \boldsymbol{\omega}_L)S(\mathbf{T}_{BR}\mathbf{y})\mathbf{T}_{BR}(\mathbf{u}_f + S(\mathbf{r}_s)\boldsymbol{\omega}_s) + S(\mathbf{T}_{BR}\mathbf{y})\mathbf{T}_{BR}(\dot{\mathbf{u}}_f + S(\mathbf{r}_s)\dot{\boldsymbol{\omega}}_s) \right) dy \\
& + \int_0^{b/2} (\rho_{w,R}(\mathbf{T}_{BR}\mathbf{J}_s\dot{\boldsymbol{\omega}}_s + S(\boldsymbol{\omega}_B + \boldsymbol{\omega}_R)\mathbf{T}_{BR}\mathbf{J}_s\boldsymbol{\omega}_s) - \tilde{m}_R S(\mathbf{T}_{BR}\mathbf{u}_f)\mathbf{T}_{BR}S(\mathbf{r}_s)\boldsymbol{\omega}_s) dy \\
& + \int_{-b/2}^0 (\rho_{w,L}(\mathbf{T}_{BR}\mathbf{J}_s\dot{\boldsymbol{\omega}}_s + S(\boldsymbol{\omega}_B + \boldsymbol{\omega}_L)\mathbf{T}_{BR}\mathbf{J}_s\boldsymbol{\omega}_s) - \tilde{m}_L S(\mathbf{T}_{BR}\mathbf{u}_f)\mathbf{T}_{BR}S(\mathbf{r}_s)\boldsymbol{\omega}_s) dy = [L \ M \ N]^T
\end{aligned} \tag{12}$$

where $\mathbf{J}_s(y) = - \int_S S^2(\mathbf{x}) dA$ denotes the second moment of area matrix of a cross section of the wing. An expression for the net moment ($[L \ M \ N]$) is given in Sec. 5.7. Note that if the terms arising from flexibility are ignored along with the wing root angular velocity, then, with the additional assumption that $\mathbf{r}_{CG} = 0$, Euler's equations are recovered as one would expect. The

equations of motion derived in this equation incorporate wing rotation (see Eq. (5) which expresses $\boldsymbol{\omega}_R$ in terms of the flapping rates) and therefore, this model can be used for a study of flexible flapping wings as well. These equations of motion can be specialized for a rigid aircraft, as described in [64].

5.5 Structural Dynamics

The bending and twisting elastic equations of motion for the right wing are given by

$$\begin{bmatrix} \tilde{m}_R & -\tilde{m}_R x_{ec} \\ -\tilde{m}_R x_{ec} & I_p \end{bmatrix} \begin{bmatrix} \dot{\mathbf{V}}_3 \\ \dot{\boldsymbol{\Omega}}_2 \end{bmatrix} + \begin{bmatrix} \eta(EI_b \dot{\xi}''')'' + (EI_b \xi''')'' - T \xi'' \\ -\eta(G\tilde{J}\dot{\theta}_s')' - (G\tilde{J}\theta_s')' \end{bmatrix} = \begin{bmatrix} \mathbf{F}_{s,3} \\ \mathbf{M}_{s,2} \end{bmatrix} \quad (13)$$

where

$$\dot{\boldsymbol{\Omega}} = \dot{\boldsymbol{\omega}}_s + \mathbf{T}_{SB}(\dot{\boldsymbol{\omega}}_B + \dot{\boldsymbol{\omega}}_R), \quad (14)$$

and

$$\begin{aligned} \dot{\mathbf{V}} &= \mathbf{T}_{SB}\dot{\mathbf{u}}_B + \dot{\mathbf{u}}_f + S(\boldsymbol{\omega}_B + \boldsymbol{\omega}_R)(\mathbf{T}_{SB}\mathbf{u}_B + \mathbf{u}_f) + \mathbf{T}_{SB}S(\boldsymbol{\omega}_B + \boldsymbol{\omega}_R)\mathbf{T}_{BR}\mathbf{u}_f \\ &\quad + \mathbf{T}_{SB}(S(\dot{\boldsymbol{\omega}}_B + \dot{\boldsymbol{\omega}}_R) + S^2(\boldsymbol{\omega}_B + \boldsymbol{\omega}_R))\mathbf{T}_{BR}\mathbf{y} \\ \xi &= \xi_f - y\delta_R \\ \mathbf{u}_f &= [0 \ 0 \ \dot{\xi}_f]^T, \end{aligned} \quad (15)$$

Remark: The displacement ξ should be viewed as comprised of the deformation ξ_f , and a rigid component, $y\delta_R$, i.e., $\xi = \xi_f(y) - y\delta_R$, with $\xi_f'(0) = 0$. This perspective is helpful from the point of view of practical implementation of boundary control schemes. Likewise, one may consider θ_s as the sum of flexible and rigid twist contributions (denoted by θ_R), instead of a pure deformation. Then, the wing may be viewed as being clamped at the root, with $\theta_s(0) = \theta_R + 0$ (zero deformation at the root). This decomposition of ξ and θ_s changes neither the governing equations nor the boundary conditions, because the rigid terms do not affect the stiffness and damping terms, while they are already incorporated into the accelerations and the right hand side.

Note that $I_p = \rho_w \mathbf{J}_s(2, 2)$ and $I_b = \mathbf{J}_s(1, 1)$, where ρ_w denotes the density of the wing. Furthermore, $\mathbf{F}_{s,3} \triangleq \mathbf{F}_{s,3}(\alpha, \dot{\alpha}, V_\infty, \mathbf{u}_f, \theta, \dot{\theta})$ is the total force acting in the local z direction (hence the subscripts ‘s’ and ‘3’), while $\mathbf{M}_{s,2} \triangleq \mathbf{M}_{s,2}(\alpha, \dot{\alpha}, V_\infty, \mathbf{u}_f, \theta, \dot{\theta})$ is the local pitching moment. The arguments of \mathbf{F} and \mathbf{M} listed here are by no means exhaustive; rather, they are the primary contributors. The term $[\dot{\mathbf{V}}]_3$ denotes the z -component of the local acceleration, and $[\dot{\boldsymbol{\omega}}]_2$ is the y -component of the local angular acceleration. Expressions for the net force and moment are given in Sec. 5.7. The Kelvin-Voigt damping coefficient is obtained by scaling EI_b and $G\tilde{J}$ by a factor of η in the bending and twist equations, respectively.

Remark: The scaling term η will not be equal for both cases, viz., bending and twist, in the most general case. Furthermore, it is common among structural dynamicists to model the damping coefficient as a linear combination of the mass (or moment of inertia) and stiffness.

Remark: The linear model presented here can be readily replaced by a nonlinear model in the proposed coordinates to match the requirements of the problem at hand.

The boundary conditions are given by the following expressions.

- At the wing root: $\xi = 0$, while ξ' and θ_s can be set arbitrarily (within admissible limits) as the dihedral angle and the twist, respectively, at the wing root.

- At the wing tip: $\xi'' = 0$, $(EI_b \xi'')' - T \xi' = 0$ and $\theta'_s = 0$ (i.e., free end boundary conditions).

Remark: If the tension T is spatially varying, i.e., $T \equiv T(y)$, then an additional term, $T' \xi'_f$, needs to be added alongside $T \xi''$ in Eq. (13).

Boundary conditions at the wing root, in particular $\theta_s(0)$ and $\xi'(0)$, can be controlled actively via dedicated actuators for stabilizing an unstable wing or for ensuring that the net force on the wing or its components achieve the desired value for specific maneuvers [63].

5.6 Fuselage Kinematics

The fuselage attitude is described by the Euler angles ψ , θ and ϕ . The kinematic equations are given by

$$\begin{aligned}\dot{\phi} &= p + q \tan \theta \sin \phi + r \tan \theta \cos \phi, \\ \dot{\theta} &= q \cos \phi - r \sin \phi, \\ \dot{\psi} &= (q \sin \phi + r \cos \phi) \sec \theta\end{aligned}\tag{16}$$

The equations which relate the position of the aircraft to its translational velocity are essentially decoupled from the flight dynamics, and are given by

$$\begin{aligned}\dot{X} &= V_{\text{gn}} \cos \gamma \cos \chi \\ \dot{Y} &= V_{\text{gn}} \cos \gamma \sin \chi \\ \dot{Z} &= -V_{\text{gn}} \sin \gamma\end{aligned}\tag{17}$$

where V_{gn} is the ground speed of the aircraft (obtained by subtracting the velocity of the wind from that of the aircraft). The flight path angle (γ) and the wind axis heading angle (χ) in Eq. (17) are defined as follows:

$$\begin{aligned}\sin \gamma &= \cos \alpha \cos \beta \sin \theta - \sin \beta \sin \phi \cos \theta - \sin \alpha \cos \beta \cos \phi \cos \theta \\ \sin \chi \cos \gamma &= \cos \alpha \cos \beta \cos \theta \sin \psi + \sin \beta (\sin \phi \sin \theta \sin \psi + \cos \phi \cos \psi) \\ &\quad + \sin \alpha \cos \beta (\cos \phi \sin \theta \sin \psi - \sin \phi \cos \psi)\end{aligned}\tag{18}$$

The turn rate is given by $\omega = \dot{\chi}$. If $\dot{\theta} = \dot{\phi} = \dot{\beta} = 0$, it follows that

$$\omega = \dot{\psi} = (q \sin \phi + r \cos \phi) \sec \theta\tag{19}$$

5.7 Forces

The net force on the aircraft consists primarily of contributions from aerodynamic and gravitational forces. For numerical analysis, the aerodynamic forces and moments are calculated using strip theory. As a method, strip theory is used for aircraft aeroelastic simulations [108] and routinely for blade element theory in the rotorcraft field [37]. Strip theory approaches have also been applied to wings in a trailing vortex flow and aircraft spin prediction (see references [50, 69, 59, 58] and others cited therein). It seems that only recently has the general strip theory approach been applied in realtime simulation for fixed-wing force and moment calculations [94, 39, 38, 83, 84]. Strip theory methods have also been applied to flapping wing aircraft [20, 46, 14].

The wing is divided into chord-wise strips. The lift, drag, and the quarter chord aerodynamic moment at each strip can be computed by using a suitable aerodynamic model, and these can be summed over the entire wing to yield the net aerodynamic force and moment. A similar calculation is performed for the horizontal tail and added to the wing contributions. The aerodynamic contributions of the fuselage are ignored with the understanding that they can be added readily to the model.

Since the model developed is intended to be as generic as possible, the model proposed by Goman and Khrabrov [29] is presented in this section as a candidate model for computing the lift and the quarter chord moment while drag is estimated assuming the classic drag polar. In the authors' estimate, Goman and Khrabrov's model offers at least two advantages over the existing models (such as Theodorsen [97] or Peters [68]). First, the model is cast in the form of a single ordinary differential equation (ODE) and two algebraic equations, one each for lift and the quarter chord pitching moment. The state variable for the ODE corresponds, physically, to the chordwise location of flow separation on the airfoil. Therefore, the model is quite easy to implement as part of a numerical routine. Second, the model is inherently nonlinear and applicable to post-stall flight.

The following equation describes the movement of the separation point for unsteady flow conditions

$$\tau_1 \dot{\nu} + \nu = \nu_0(\alpha - \tau_2 \dot{\alpha}) \quad (20)$$

where ν denotes the position of the separation point, τ_1 is the relaxation time constant, and τ_2 captures the time delay effects due to the flow, while ν_0 is an expression for the nominal position of the separation point. These three parameters need to be identified experimentally or using CFD for the particular airfoil under consideration. The coefficients of lift and quarter-chord moment are then given by

$$\begin{aligned} C_l^* &= \frac{\pi}{2} \sin(\alpha(1 + \nu + 2\sqrt{\nu})) \\ C_{m_{ac}}^* &= \frac{\pi}{2} \sin(\alpha(1 + \nu + 2\sqrt{\nu})) \left[\frac{5 + 5\nu - 6\sqrt{\nu}}{16} \right] \end{aligned} \quad (21)$$

The lift force and the quarter chord moment per unit span are then given by

$$\begin{aligned} L(y) &= 0.5\rho V(y)^2 c C_l^* + \frac{\pi}{4} \rho c^2 \left(\ddot{\xi} + V_\infty \dot{\alpha} - (x_a - 0.25)c\ddot{\alpha} \right) \\ M(y) &= 0.5\rho V(y)^2 c^2 C_{m_{ac}}^* + \frac{\pi}{4} \rho c^2 \left(V_\infty \dot{\xi} + \frac{(x_a - 0.25)c\ddot{\xi}}{2} + V_\infty^2 \alpha - c^2 \left(\frac{1}{32} + (x_a - 0.25)^2 \right) \ddot{\alpha} \right) \end{aligned} \quad (22)$$

where α is the local angle of attack, and ρ denotes the density of air. Furthermore, $V = \|\mathbf{V}\|$ is the local wind speed with \mathbf{V} defined in Eq. (6), and V_∞ is the freestream speed of the aircraft given by $V_\infty = \|\mathbf{u}_B\|$. The last term of each expression was added to Goman's original model [29] and corresponds to the apparent mass effect [20].

There is, unfortunately, no simple expression for the sectional drag coefficient. The sectional drag coefficient can be written as

$$C_d = \frac{0.664}{\sqrt{Re}} + \frac{1}{\pi e A_R} C_l^2, \quad (23)$$

where $C_l = \frac{L(y)}{0.5\rho V(y)^2 c}$, A_R is the aspect ratio of the wing, Re denotes the chordwise Reynolds

number, and e is Oswald's efficiency factor. The skin friction term [45] assumes laminar flow over the wing and may need to be replaced with a different approximation (see DeLaurier [20] for instance). The drag model is quasi-steady in nature so that dynamic stall effects are not included. A refined model for calculating drag, incorporating dynamic stall, may be found in DeLaurier [20].

The local aerodynamic force on each wing can be written in the body axis system

$$\begin{bmatrix} X_A(y) \\ Y_A(y) \\ Z_A(y) \end{bmatrix} = \mathbf{T}_{BS} \begin{bmatrix} L(y) \sin \alpha(y) - D(y) \cos \alpha(y) \\ 0 \\ -L(y) \cos \alpha(y) - D(y) \sin \alpha(y) \end{bmatrix} \quad (24)$$

Note that \mathbf{T}_{BS} is used instead of \mathbf{T}_{BR} and this is the most important source of the difference between the resultant of the forces and moments on a flexible wing vis-a-vis a rigid wing. The components of the gravitational force are given by

$$X_g = -mg \sin \theta, \quad Y_g = mg \cos \theta \sin \phi, \quad Z_g = mg \cos \theta \cos \phi \quad (25)$$

and the corresponding moment is given by $S(\mathbf{r}_{cg})[X_g \ Y_g \ Z_g]^T$.

The net aerodynamic force on two wings is given by

$$\begin{bmatrix} X_B \\ Y_B \\ Z_B \end{bmatrix}_{\text{wing}} = \int_0^{b/2} \begin{bmatrix} X_A(y) \\ Y_A(y) \\ Z_A(y) \end{bmatrix}_{\text{right}} dy + \int_0^{b/2} \begin{bmatrix} X_A(y) \\ Y_A(y) \\ Z_A(y) \end{bmatrix}_{\text{left}} dy \quad (26)$$

The net aerodynamic moment due to the two wings is given by

$$\begin{bmatrix} L \\ M \\ N \end{bmatrix}_{\text{wing}} = \int_0^{b/2} S(\mathbf{y}) \begin{bmatrix} X_A(y) \\ Y_A(y) \\ Z_A(y) \end{bmatrix}_{\text{right}} dy + \int_0^{b/2} S(\mathbf{y}) \begin{bmatrix} X_A(y) \\ Y_A(y) \\ Z_A(y) \end{bmatrix}_{\text{left}} dy \quad (27)$$

A similar calculation can be performed for the horizontal tail. The net force and moment on the aircraft themselves are the sum of the contributions from the wing, the horizontal tail and gravity:

$$\begin{aligned} \begin{bmatrix} X_B \\ Y_B \\ Z_B \end{bmatrix} &= \begin{bmatrix} X_B \\ Y_B \\ Z_B \end{bmatrix}_{\text{wing}} + \begin{bmatrix} X_B \\ Y_B \\ Z_B \end{bmatrix}_{\text{tail}} + \begin{bmatrix} X_g \\ Y_g \\ Z_g \end{bmatrix} \\ \begin{bmatrix} L \\ M \\ N \end{bmatrix} &= \begin{bmatrix} L \\ M \\ N \end{bmatrix}_{\text{wing}} + \begin{bmatrix} L \\ M \\ N \end{bmatrix}_{\text{tail}} + S(\mathbf{r}_{cg}) \begin{bmatrix} X_g \\ Y_g \\ Z_g \end{bmatrix} \end{aligned} \quad (28)$$

This completes the formulation of the equations of motion.

5.8 Aerodynamic Model for Trim Calculations

The lift and drag coefficients of the wing and tail airfoils, adapted from values determined experimentally [100] for the Vapor airplane itself at a Reynolds number of 20000, are given by

$$C_L = 0.28295 + 2.00417\alpha, \quad C_D = 0.0346 + 0.3438C_L^2, \quad (29)$$

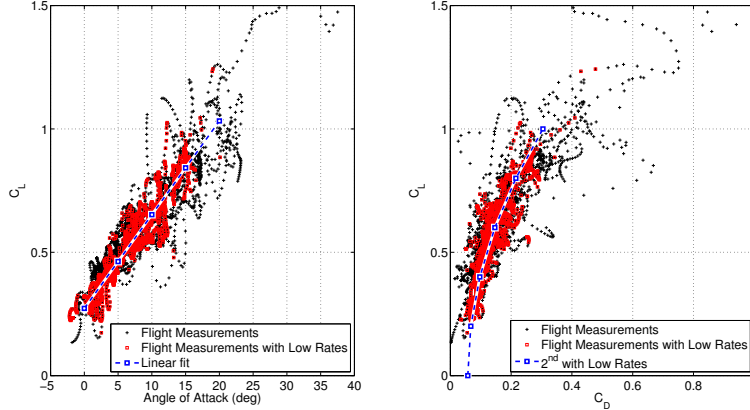


Figure 6: Experimentally obtained aerodynamic data [100].

where α is measured in radians. Using thin airfoil theory [49], it was determined that $C_{mac} = -0.1311$. The actual experimental plot has been shown in figure 6. The C_L and C_D expressions in equation (29) are obtained by averaging *only* over the red points in figure 6. The rest of the points in figure 6 (marked in black) represent data collected at high values of pitch rate and $\dot{\alpha}$, and are not relevant to the discussion. During the experiments, for $\alpha > 25$ deg, $\dot{\alpha}$ was seen to be substantial, and therefore, the coefficients in equation (29) are reliable only up to $\alpha = 25$ deg.

The aircraft weighs 12 grams, including a ballast mass added to the nose of the aircraft for placing the CG around half-wing-chord under nominal conditions; i.e., when the wing dihedral and incidence are both zero. The aircraft is 29.7 cm long from nose to tail, and under nominal conditions, the distance between the AC and the CG is $x_{ac} = 3.6$ cm. The horizontal tail is located 26.1 cm behind the wing root AC. The limiting value of the horizontal tail deflection is assumed to be 30 deg in both directions. The limiting value of the wing dihedral is assumed to be 60 deg on either side, while that of the wing incidence is 15 deg.

6 Performance and Stability of a Rigid Aircraft

6.1 Comparison With the Vertical Tail

Figure 7 illustrates the physics underlying the use of wing dihedral as a control. Increasing the wing dihedral reduces the force acting in the body z -direction, and generates a side force. The reduced z -force affects the aircraft flight path angle and angle of attack, and hence the flight speed. On the other hand, the side force can be used for providing the centripetal force for turning, and as a source of the yawing moment. In particular, if the CG is located behind the line of action of the side force, then a positive side force produces a positive yawing moment and vice-versa (see figure 5 for the sign conventions). It follows that a positive rolling moment (wherein the lift on the left wing is higher than the right wing) is accompanied by a positive yawing moment if the wings have a positive dihedral deflection. Consequently, the adverse yaw produced due to rolling is reduced.

Assuming a linear relation between the lift and the angle of attack, the yawing moment generated

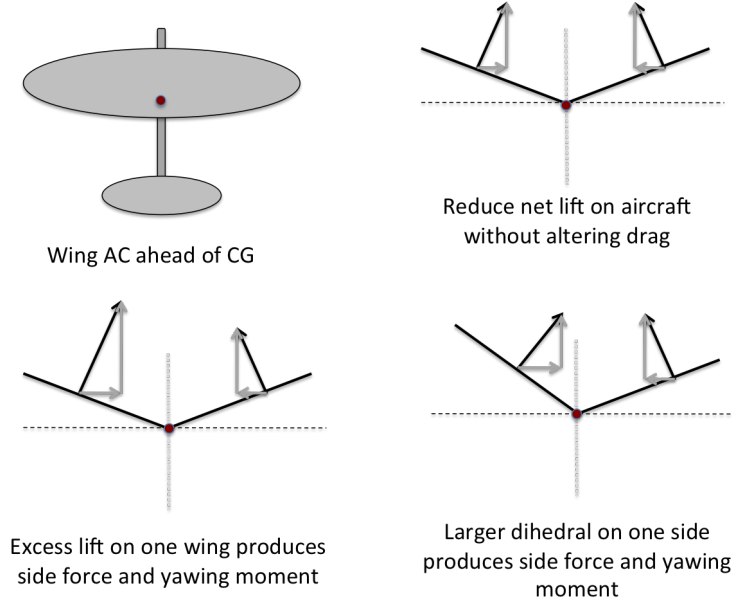


Figure 7: Illustration of the physics underlying the use of dihedral as a control. The dark conspicuous dot in the figures is the aircraft CG.

by a dihedral deflection δ of the left wing, while that of the right wing is zero, is given by

$$N_w = q_\infty S_w (l_w C_{L\alpha} \alpha + c C_{m_{ac}}) \delta \quad (30)$$

Clearly, the dihedral is more effective for yaw control at high angles of attack. Equation (30) also suggests that the dihedral is better than the vertical tail when l_t is small. The ability to change wing dihedral is built into birds in the form of their ability to flap their wings for propulsion. Hence, no additional mechanisms are needed for yaw control. Ornithopters, too, can benefit from differential dihedral-based yaw control in a similar manner.

For positively cambered wings, $C_{m_{ac}} < 0$. Hence the second term on the right hand side of (30) is negative and not only reduces ζ , but could also render it negative. This leads to the problem of *reversal of control effectiveness* (measured by the sign of N_w in equation (30)).

Figure 8 plots the sign of the control effectiveness, i.e., $\text{sign}\left(\frac{\Delta N}{\Delta(\delta_L - \delta_R)}\right)$, on a $p-r$ grid for $\alpha = 8.595$ deg (0.15 rad). The plot clearly shows that the sign of the control effectiveness depends strongly on the angular rates. Moreover, as shown in [64], it is uniformly negative for $\alpha < 6$ deg and uniformly positive for $\alpha > 12$ deg. The sign of the control effectiveness is usually assumed to be known *a priori* while designing control laws. The challenge involved in designing a sound turning flight controller is captured in figure 8.

6.2 Analytical Approximations to Lateral-Directional Stability

The lift and drag forces produced by the wing as well as their moments about the origin of the body frame can be resolved along the body axes. In particular, summing the body axis components of the net moment due to lift and drag yield the net rolling, pitching and yawing moments. Stability

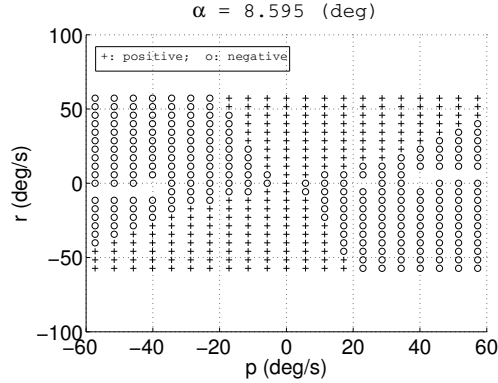


Figure 8: Plot showing the sign of the control effectiveness, $\text{sign}\left(\frac{\Delta N}{\Delta(\delta_L - \delta_R)}\right)$ as a function of roll rate and yaw rate at $\alpha \approx 8.5$ deg.

of aircraft depends primarily on the three aerodynamic moments and their derivatives with respect to the aircraft angular velocity, angle of attack and sideslip.

Table 1: Stability derivatives for a tailless aircraft with an articulated wing

Derivative	Symmetric flight ($\delta_L = \delta_R = \delta$)	Turning flight ($\delta_L \approx -\delta_R$)	Stability condition
L_β	Stable	Stable when $\delta_L + \delta_R > 0$	$L_\beta < 0$
L_p	Stable	Stable	$L_p < 0$
N_β	Unstable	Unstable	$N_\beta > 0$
N_r	Stable (drag reduces stability)	Unstable, but stable when $\text{sign}(p) \neq \text{sign}(\delta_L - \delta_R)$	$N_r < 0$

Table 1 lists some stability derivatives, and their qualitative properties for a tailless articulated wing aircraft. Based on the results in table 1, it is clear that the aircraft would be expected to be unstable in most flight regimes. At least two stability derivatives suggest the possibility of stability in some select turn regimes. However, in rapid turn regimes, the flight dynamics are far too strongly coupled to draw reliable conclusions from linear, decoupled analysis. Furthermore, because the stability derivatives depend strongly on the wing dihedral angle, which is in turn a function of the aircraft maneuver, it follows that stability is tied very closely to the nature of the maneuver being executed. The observation is peculiar to aircraft with articulated wings. In conventional aircraft with fixed wings, although stability derivatives depend on aircraft states, they are essentially independent of the control surface deflection.

The idea of using wing dihedral for control is particularly useful when the wings are flexible, because flexible wings bend and twist spontaneously under aerodynamic loading. The dihedral angle at a given point on the wing is equal to the sum of the slope of the bending displacement and the wing slope at the root. Since bending and twisting are coupled, wing twist can be used to bring about a passive proverse change in the wing dihedral.

7 Analysis of the Wing and Effective Dihedral

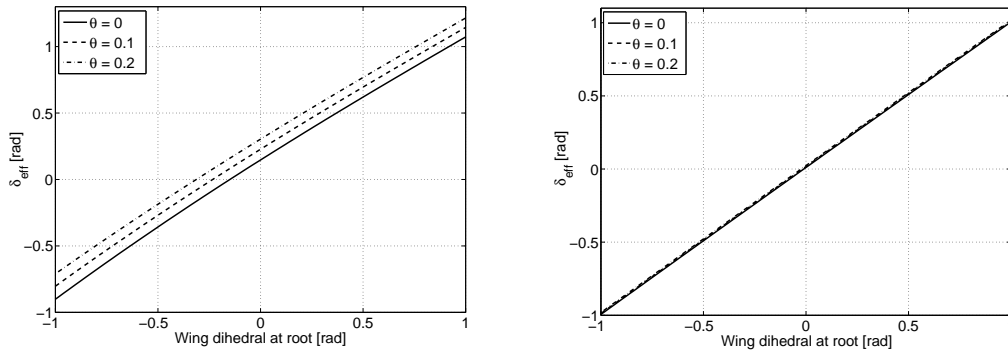
7.1 Effective Dihedral

The Young's modulus of the wing, E , may be considered as a design parameter. In order to exploit the idea of using the wing dihedral for yaw control, the wing dihedral effect itself may be looked upon as a design driver for E .

The role of differential (or asymmetric) dihedral for yaw control has been discussed in detail in Ref. [64]. The dihedral primarily produces a side force, which is actually a component of the total force produced by the wing normal to its local plane. Let Y_A and Z_A denote the local forces produced by the wing along the body y and z axes, respectively. Therefore, one may define a term called the effective dihedral, δ_{eff} , as follows:

$$\delta_{\text{eff}} = \tan^{-1} \left(\frac{\int_0^{b/2} Y_A(y) dy}{\int_0^{b/2} Z_A(y) dy} \right) \quad (31)$$

This notion of effective dihedral is different from, and arguably more general than, that of Rodden [77] who derived expressions for the increments, arising from the wing bending, in the rolling moment derivatives. The notion of effective dihedral is particularly useful for wing design from the point of view of elasticity. The Young's modulus, E , could be chosen to ensure that the wing produces a sufficient effective dihedral effect with reasonable actuator forces. The effective dihedral depends on the boundary conditions to which the wing is subjected whereas the boundary conditions themselves depend on the location and type of actuators. For a rigid wing, the effective dihedral and the actual dihedral are equal.



(a) Effective dihedral when $E = 5$ MPa.

(b) Effective dihedral when $E = 50$ MPa.

Figure 9: Effective dihedral as a function of the dihedral angle at the wing root for two different values of the Young's modulus. Each plot shows the effective dihedral for three values of wing tip twist (θ): 0, 0.1 rad and 0.2 rad. This plot was obtained for $V = 2.5$ m/s and $\alpha = 10$ deg.

Figures 9(a) and 9(b) show the effective dihedral as a function of the wing dihedral angle at the root. The effective dihedral, as expected, is much higher for $E = 5$ MPa as compared to $E = 50$ MPa. In the former case, the wing bending is large enough so that the flexibility provides a substantial increase in the wing dihedral effect. This suggests that for the particular wing geometry

considered here, a material with a Young's modulus of $E \sim \mathcal{O}(1)$ MPa should be chosen in order to obtain a significant dihedral effect. This conclusion depends on other chosen parameters and hence, such analysis should be performed on a case-by-case basis. Furthermore, it is important to note that the effective dihedral depends on the trim condition under consideration.

The effective dihedral is useful in another way. It forms the basis to extend the stability analysis for a rigid aircraft to the case of flexible wings. In Ref. [64], for example, analytical expressions for the traditional lateral stability derivatives were obtained for a rigid aircraft and the stability of lateral-directional modes was examined for various values of the wing dihedral. Those results would be applicable to a flexible-winged aircraft when the effective dihedral angle of the wing is matched to the dihedral angle of a rigid wing. This is valid regardless of the deformation profile of the wing. For the aircraft model considered here, it suggests that the motion stability would be similar to that of the rigid aircraft when $E \geq \mathcal{O}(10)$ MPa.

7.2 Bending and Twist Natural Frequencies

Traditionally, natural frequencies of lifting surfaces are defined in terms of inertia and elastic stiffness. However, unsteady aerodynamic lift and moment relations contain terms which mathematically play the same role as stiffness, damping, and inertia in the governing relations. Consequently, another set of natural pseudo frequencies can be defined which include these aerodynamic contributions.

Consider the case where $\theta'(b/2) = \xi''(b/2) = \xi'''(b/2) = 0$. If ω_θ and ω_ξ denote the frequencies of the first (decoupled) twisting and bending modes, respectively, then it can be shown that [6]

$$\omega_\theta^2 = \frac{\pi^2}{4L^2} \frac{G\tilde{J}}{I_p} - \frac{M}{I_p}, \quad \omega_\xi^2 = \frac{12.36}{L^4} \frac{EI_b}{m} \quad (32)$$

where M denotes $\frac{\partial \mathbf{M}_{s,2}}{\partial \theta}$ (linearized twisting moment). In order to estimate the extent of time-scale separation, the ratio $\omega_\theta^2/\omega_\xi^2$ is of interest. Time-scale separation is a property wherein the dynamics consist of two sets of modes, one of which is significantly (at least an order of magnitude) faster than the other mode. The stability of each mode can then be analyzed independently, with other mode contributing a constant term whose value is a function of the mode being analyzed [1].

It can be shown that the time scale separation between bending and twisting depends primarily on the aspect ratio, the flight speed and the geometry of the wing cross section. The ratio $\omega_\theta^2/\omega_\xi^2$ is given by [62, 63]

$$\frac{\omega_\theta^2}{\omega_\xi^2} \approx 3 \frac{G}{E} \frac{L^2}{c^2} \approx \frac{3}{2(1+\nu_p)} \frac{L^2}{c^2} \quad (33)$$

where ν_p is Poisson's ratio. The ratio $1.5/(1+\nu_p) \approx 1$. Therefore,

$$\frac{\omega_\theta}{\omega_\xi} \approx \mathcal{O}(L/c) \quad (\text{the aspect ratio of the wing})$$

Therefore, the twist dynamics are faster than the bending dynamics. The time scale separation reduces with decreasing E and increasing V , as the influence of the aerodynamic terms increasingly dominates the contribution from elasticity. The time scale separation increases with increasing

aspect ratio. Although this time scale separation cannot be used to draw any inference about the susceptibility of the wing to flutter, it can be used as the basis for designing independent controllers for controlling wing bending and torsion. Time scale separation is used quite commonly in flight control design in a similar fashion [89, 103, 73, 35]. Incidentally, equation (33) suggests that significant time scale separation is to be expected in slow aircraft with large aspect ratio wings, such as gliders and high altitude, long endurance aircraft like the NASA HALE [71, 72].

8 Bifurcation Analysis of Turning Flight

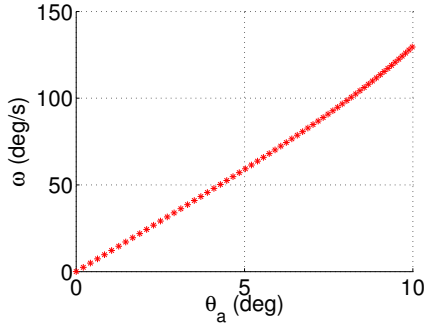
The performance and stability of an MAV equipped with flexible wings ($E = 5$ MPa) in steady turning flight is analysed in a manner similar to that described for a rigid aircraft in Ref. [64]. A similar analysis could be repeated for other maneuvers of interest. Insofar as turning is concerned, wing flexibility may have one or more of several possible consequences.

1. The overall turn rate may improve because of the additional dihedral generated by the flexible wings.
2. Alternately, for a given turn rate, the dihedral angles required at the wing root would be reduced.
3. When the sideslip is not deliberately regulated, it would be reduced due to the enhanced dihedral effect.

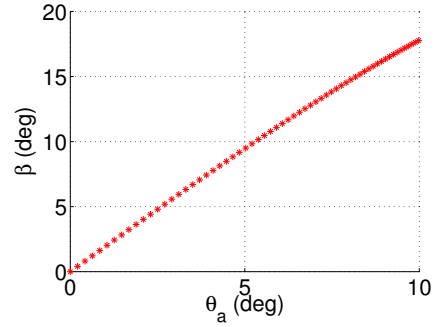
It turns out that flexibility does result in a net improvement in the turn rate of the aircraft, but only when wing incidence angle at the root (or wing twist in general) is used actively. There is a significant reduction in the sideslip when the wings are locked in a symmetric dihedral configuration. However, when the dihedral angles alone are used for turns, the maximum achievable turn rate does not improve vis-a-vis a rigid aircraft. Furthermore, the magnitude of the commanded dihedral deflections required for a given turn rate is reduced in comparison to an aircraft with rigid wings. The complete set of trim analysis may be found in [64, 62], while some sample cases are presented here.

8.1 Reduction in Sideslip (Variable θ_L ; $\theta_R = -\theta_L = -\theta_a$; $\delta_L = \delta_R$)

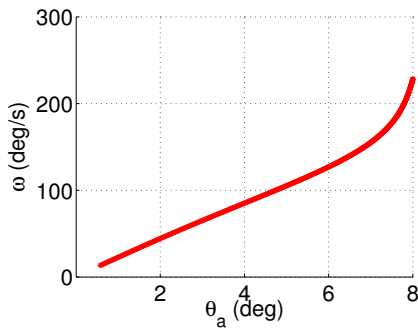
A turn is usually initiated by rolling the aircraft to the appropriate bank angle and followed by providing the appropriate yaw rate and pitch rate. When the flexible wings are twisted asymmetrically, the resultant roll rate causes a build-up in yaw rate due to the dihedral effect. However, if the wings are locked in a symmetric dihedral configuration, the resultant turn is accompanied by a sideslip which increases with increasing turn (roll) rate. This phenomenon has been captured in Fig. 10 where the dihedral angle at the root was set to 29 deg (0.5 rad) for both wings. The equilibrium points are marked with a red asterisk '*', indicating that they are unstable with a single positive real eigenvalue. For a rigid wing, the sideslip remains less than 5 deg until the turn rate builds up to 35 deg/s (compared with nearly 70 deg/s for flexible wings). Thereafter, the aerodynamic data used here is insufficient to provide accurate trim results. In general, though, the sideslip increases with increasing turn rate for an aircraft with a rigid wing. On the other hand, when the wings are flexible, the turn rate increases sharply with increasing wing twist and furthermore, the sideslip peaks at just over 10 deg and drops thereafter due to the increasing effective dihedral angle. With



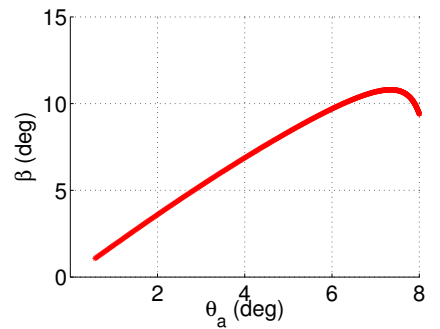
(a) Turn rate for the rigid wing aircraft



(b) Sideslip for the rigid wing aircraft



(c) Turn rate for the flexible wing aircraft



(d) Sideslip for the flexible wing aircraft

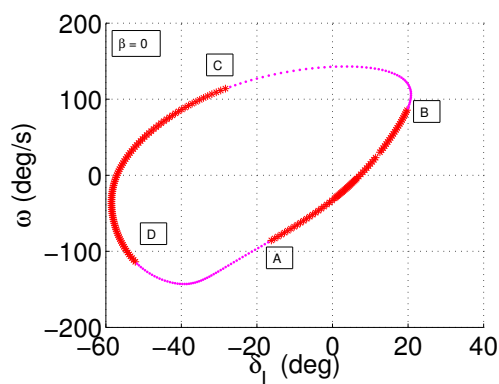
Figure 10: A comparison of the sideslip and turn rate as functions of anti-symmetric wing twist for otherwise identical airframes equipped with rigid and flexible wings. The wings have a Young's modulus of 5 MPa. The equilibria are marked with a red asterisk to denote that the Jacobian has a single positive real eigenvalue. In both cases, the dihedral angle at both wing roots was set to 25 deg. The flight speed was set to 2.8 m/s and the elevator was fixed at -11 deg and $\delta_L = \delta_R = 29$ deg (0.5 rad).

aerodynamic data that is accurate for larger values of sideslip, the value of sideslip at the peak is liable to shift from that obtained with the present model. However, the peak itself occurs due to a favourable yawing moment which comes with an increasing wing dihedral. Therefore, a peak would be expected even with improved aerodynamic data, unless adverse yawing moment from the fuselage causes the sideslip to keep increasing with the turn rate.

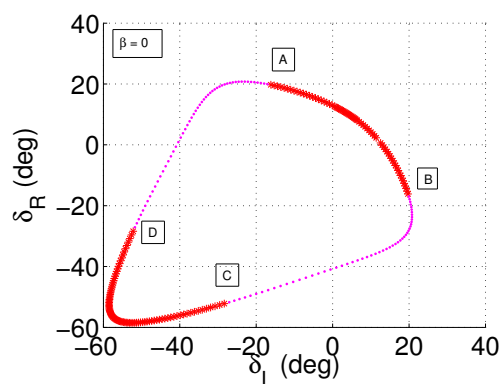
It is of interest to note that the topology of the equilibrium surface depends strongly on the wing dihedral. If the root dihedral angles are set to zero, a qualitatively different picture emerges as shown in [62]. Therefore, the open-loop behavior needs to be understood thoroughly before a turning controller is designed.

8.2 Coordinated Turn ($\theta_L = \theta_R = 0$; δ_L, δ_R variable)

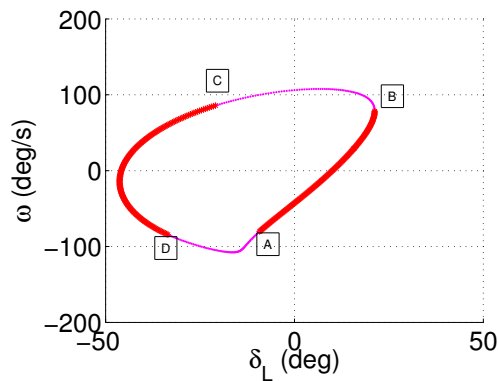
Figure 11 compares the turning performance an aircraft equipped with rigid wings with that of one equipped with flexible wings with Young's modulus $E = 5$ MPa when the sideslip is required to be regulated to $\beta = 0$. The twist angle at each wing root is set to zero, i.e., $\theta_R = \theta_L = 0$. It is clear that there is no appreciable increase in the maximum achievable turn rate. However, a noticeably smaller dihedral deflection is required at the wing root for a given turn rate when the wings are flexible, as expected. The stability characteristics seen for the two sets of aircraft are identical. The



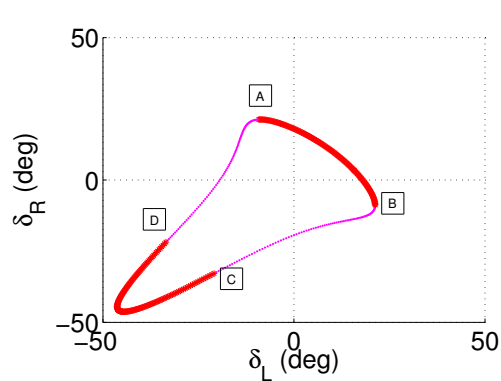
(a) Turn rate for the rigid wing aircraft



(b) Right wing dihedral angle for the rigid wing aircraft



(c) Turn rate for the flexible wing aircraft



(d) Right wing dihedral angle for the flexible wing aircraft

Figure 11: A comparison of the turn rate as a function of the left wing dihedral angle, and the right wing dihedral angle required to maintain zero sideslip, for otherwise identical airframes equipped with rigid and flexible wings. In both cases, the elevator deflection was fixed at -11 deg, and $\theta_R = \theta_L = 0$. The flexible wings have a Young's modulus of 5 MPa. The Jacobian of equilibria marked by pink dots have three eigenvalues with positive real parts: one real and a complex conjugate pair. The flight speed and angle of attack are within the range of validity of the aerodynamic data.

points marked A, B, C and D are all Hopf bifurcations. Evidently, none of the computed equilibria possess inherent stability.

Remark: It was seen in Sec. 8.1 that the turn rate improved for a flexible wing MAV, accompanied by a reduced sideslip. On the other hand, in the present section, there is a deterioration in the coordinated turn performance, measured by the maximum turn rate, when the wings are flexible. This can be explained as follows. At the angle of attack considered here, the wing twists upward (i.e., the leading edge goes up) so that the net angle of attack on the wing is higher than in the rigid case. Therefore, for a given tail setting, the aircraft flies at a lower flight speed to maintain trim in pitch. The reduced speed leads to a reduction in the net lift, which, in turn, reduces the amount of centripetal force available to sustain rapid turns. Another point worth noting is that the maximum achievable turn rate depends on the maximum achievable yawing moment. The yawing moment for a given wing incidence setting reaches a maximum when the wing dihedral angle is 45 deg, or when the effective dihedral of a flexible wing equals 45 deg. This sets another fundamental limitation on the maximum achievable turn rate, and one that arises out of the sole use the wing dihedral for turning.

8.3 Discussion

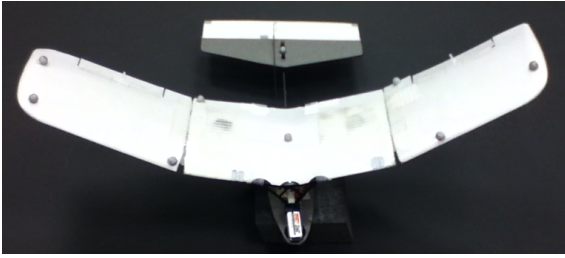
The results presented above yield some interesting design pointers. The wing flexibility can be reduced significantly (up to $\mathcal{O}(10)$ MPa for the wing geometry and flight speeds considered here) without achieving a substantial improvement in the coordinated turn rate or any measurable change in the effective dihedral angle, although a considerable saving in the wing mass can be achieved in the process. The motion stability (notwithstanding the structural stability of the wing) will not be markedly different from that of a rigid configuration. One interpretation which follows is that flexibility offers only a limited improvement in the performance, notwithstanding savings on the wing mass. Alternately, a complete aeroelastic analysis can be bypassed as long as the flutter and divergence speeds are “considerably larger” than the prescribed flight speeds (see Sec. 7.2).

These conclusions are, by no means, universally valid but, when used judiciously, can achieve considerable savings in the computational effort invested in the design. In a recent paper, Baghdadi, Lowenberg, and Isikveren [3] observed that the open loop stability characteristics did not change markedly between the rigid and flexible configurations considered in their paper. This is in keeping with the observations in this AFOSR project. Nevertheless, a control law designed using a rigid model yielded markedly different closed loop stability characteristics when the time constants of the rigid and flexible modes were close to each other. On similar lines, Merrett and Hilton [53] demonstrated that flutter (motion instabilities) can arise in high-speed aircraft due to transient maneuvers such as accelerations or rapid, instantaneous turns.

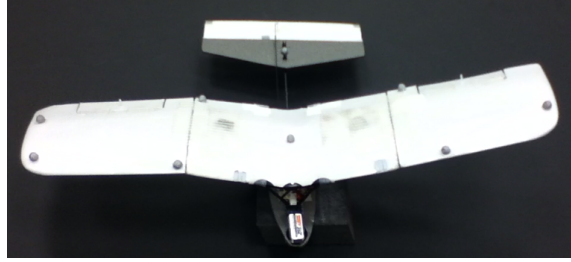
9 Experiments, Control Design and Perching

The purpose of the experiments was (a) to design control laws for an articulated wing aircraft, and (b) to implement them with a view of understanding their effectiveness as well as limitations. This section also discusses the perching maneuver, which is one of the most important maneuvers a flapping-wing aircraft would be expected to execute in the gliding phase. Further details on the experiments may be found in [26].

The experiments described here were performed on a test MAV, shown in Figure 12, which is a



(a) Symmetric dihedral 40 degrees



(b) Asymmetric configuration

Figure 12: Representative configurations showing the asymmetric dihedral capability of the wings. The foam table on which the aircraft is resting is not part of the airframe.

modified version of the commercially manufactured ParkZone Ember 2. The aircraft weighs 44 g, and has a wing span of 42 cm with an aspect ratio of 4.5. The outboard sections of both wings were free to rotate from a maximum 45 deg dihedral to minimum -15 deg anhedral for a total arc range of 60 deg. The actuators for wing dihedral, it may be recalled, are controlled independently on both wings for yaw stability and control. The VICON motion-capture system, consisting of 16 infrared cameras, was used to collect flight data, in particular the aircraft position and spatial orientation, at 100 Hz.

9.1 Control Law Design

Control law design for the MAV is described in this section. The control law has a two-tier hierarchical structure based on time-scale separation [103] which occurs naturally between the fast rotational dynamics and the slow translational dynamics:

- The innermost loop commands the elevator and the asymmetric components of the wing dihedral.
- The outer loop commands the angle of attack and turn rate to be tracked by the inner loop based on flight speed and turn rate. The turn rate and the flight path angle are computed based on position measurements.

A schematic of the controller is shown in Fig. 13.

The control design used for experiments can be justified using the dynamic inversion (DI) approach presented by Hovakimyan, Lavretsky and Sasane [35]. In [26], we argued that the DI-based controller can be simplified to standard PI(D) controllers, and exact gain tuning laws are derived in the process. The point to be noted here is that PI and PID controllers can be used for nonlinear systems. Singular perturbation theory can be used to show that the tracking error bound is of the order $1/\epsilon$ [35]. To address robustness concerns, a filter can be added in line with the small gain theorem. This is done in adaptive control methodologies where, instead of substituting for $f(t, x, u)$ with \dot{x} , $f(t, x, u)$ is predicted online using adaptive algorithms [60].

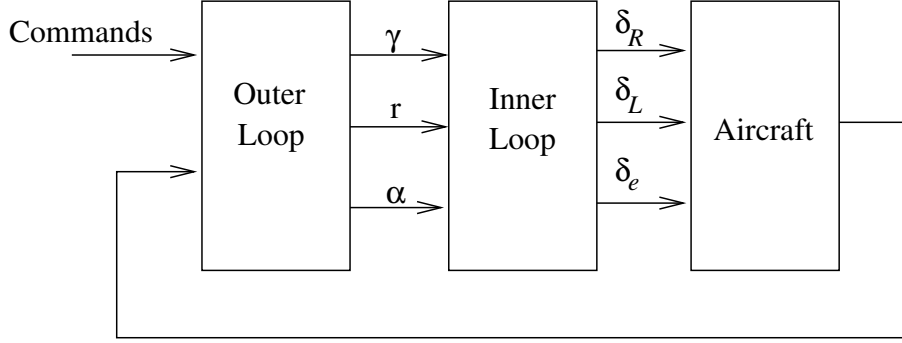


Figure 13: Schematic of the controller, where χ denotes the aircraft heading.

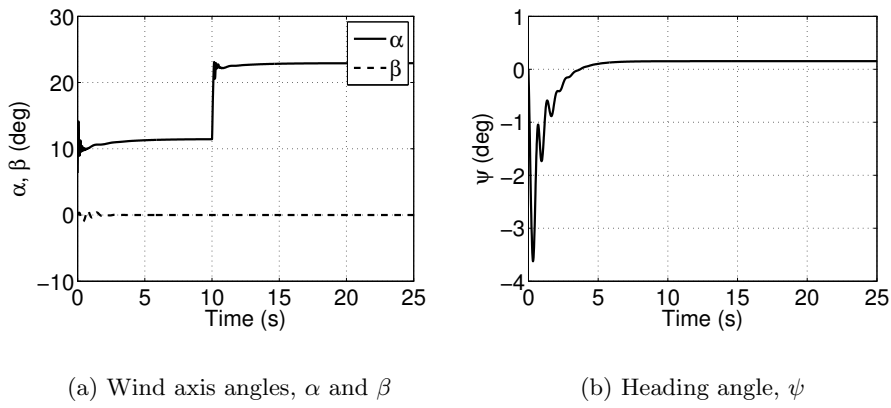


Figure 14: Simulated time histories of the aircraft in a disturbance-free flight. A 12 deg (0.2 rad jump in the angle of attack, α , is commanded. The resulting disturbances are rejected by the control law.)

9.2 Simulations

PID controllers designed using DI-inspired tuning were simulated. The time histories obtained in two different environments have been plotted in Figs 14 (no external disturbances) and 15 (persistent periodic disturbances). In both cases, the controllers performed satisfactorily. The angle of attack was kept above 11 deg to ensure the yaw control effectiveness of the dihedral was uniformly positive.

The purpose of the simulations was to demonstrate a general control design technique. However, in the course of experiments, we were able to make reasonable estimates of the open loop dynamics. This allowed us to tune controllers without resorting to a DI-inspired scheme.

The longitudinal dynamics of the aircraft were seen to be stable, but poorly damped for $\alpha > 8$ deg. Around $\alpha = 15$ deg, the elevator effectiveness saturated and higher angles of attack were unattainable under steady state conditions. The open loop response was measured to have a time period of 1 s. The observed reduction in the amplitude of oscillations was used to approximate the

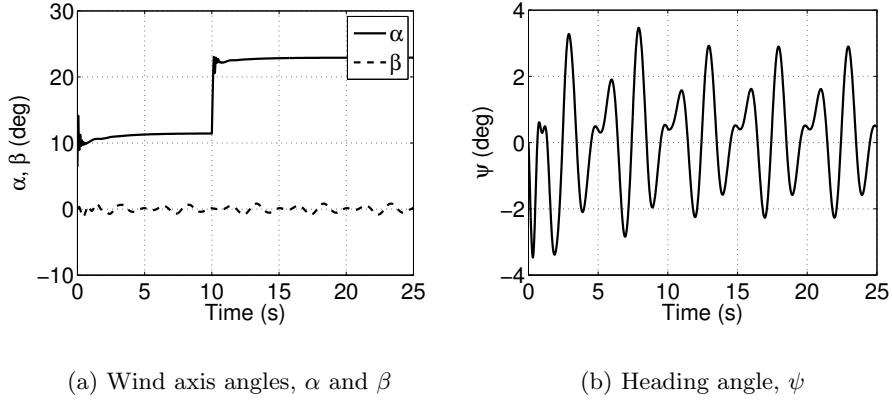


Figure 15: Simulated time histories of the aircraft in a persistent periodic lateral-directional disturbance field. A 12 deg (0.2 rad jump in the angle of attack, α , is commanded.)

damping coefficient to 0.046. The open loop dynamics can be written in the form

$$\ddot{\alpha} + 0.62\dot{\alpha} + 40\alpha = -40\delta_e + 5.6 \quad (34)$$

Therefore, an essentially derivative-integral controller was designed for the tailless configuration:

$$\delta_e(t) = 0.14 - \alpha_c + k_d \dot{e} + k_i \int_0^t e_\alpha dt, \quad (35)$$

where the offset of 0.14 rad was added based on the measured $\delta_e - \alpha$ trims. The gain k_i was similar to that for the configuration with a vertical tail, while $k_d = 0.217$ is chosen so that the damping coefficient is approximately equal to 0.7.

Based on experimental observations, it was estimated that the open loop yaw-rate dynamics are of the form

$$\ddot{r} + 2\zeta\omega\dot{r} + \omega^2 r = N_{\delta_{\text{asym}}} \delta_{\text{asym}}, \quad \zeta \approx -0.1, \quad \omega \approx 2\pi \quad (36)$$

for $\alpha < 8$ deg. Thereafter, the yaw dynamics are unstable and oscillatory in nature. In order to account for the actuator time delay of 0.2 s, a lead compensator $L(s)$ was designed given by $L(s) = \frac{8(s+4.5)}{4.5(s+8)}$. The role of dihedral control is regulation, and it suffices use a derivative controller

for damping addition, with the derivative filter given by $D(s) = \frac{12(s+4)}{s+8}$. The commanded anti-symmetric dihedral deflection is given by

$$\delta_{\text{asym}} = k_d D(s) L(s) e_r(s) \quad (37)$$

9.3 Perching Guidance Loop

The outer control loop is designed to ensure rapid changes in the flight path over a short duration. The flight path angle is controlled in discrete time so that a symmetric dihedral angle is commanded every 0.2 s (which is equal to the dihedral acutator time delay). The commanded dihedral angles

are given by

$$\delta_R = \delta_L = \sqrt{2 + \frac{2}{f(\alpha) \tan \gamma_c}}, \quad f(\alpha) \approx \frac{C_L(\alpha)}{C_D(\alpha)} \quad (38)$$

where γ_c is the commanded flight path angle which is, in turn, given by

$$\gamma_c = \tan^{-1}(h) \approx \frac{h}{1 + 0.28125h^2}, \quad h = \frac{z - z_l}{\sqrt{(x - x_l)^2 + (y - y_l)^2}} \quad (39)$$

Here, x_l , y_l and z_l are the coordinates of the desired landing point on the ground, or a point in the air where a perching command is to be sent to the aircraft. This simple controller was seen to be quite effective over the short duration of the experiments.

9.4 Angle of Attack Control for Perching

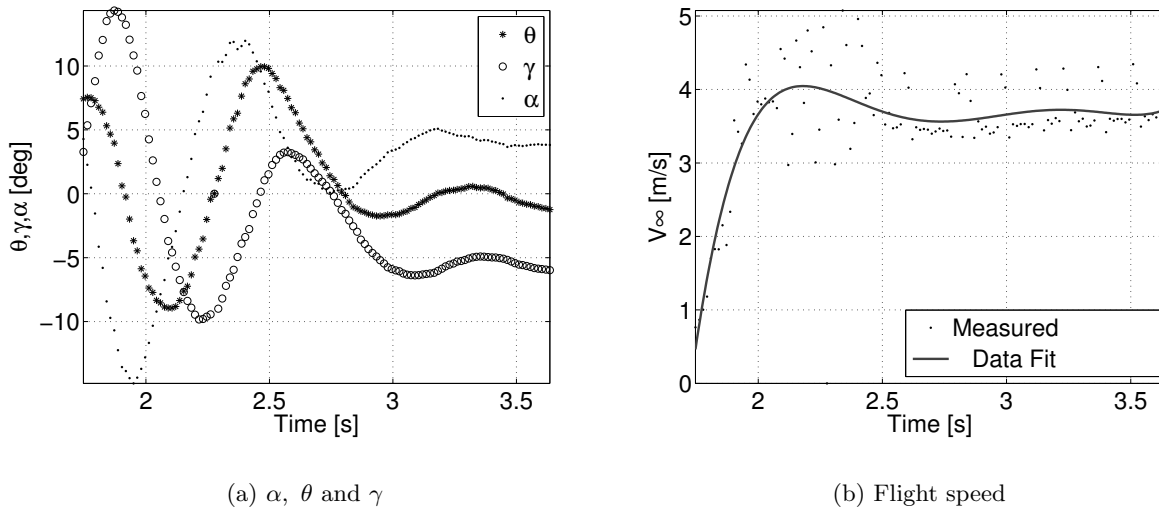


Figure 16: Experimental results showing the longitudinal flight parameters. In particular, α settles down at the desired value within 2 s.

Figure 16 shows the experimentally-measured longitudinal flight parameters. For these experiments, the wing dihedral was not controlled actively which caused the aircraft heading to deviate steadily from a straight line. An angle of attack of 5 deg was commanded while the flight speed and flight path angle were not controlled. The controller for the tailless aircraft yielded similar characteristics as the one with a vertical tail.

9.5 Lateral-Directional Control for Perching

In the aircraft with a vertical tail, local lateral stability was achieved using a simple PID controller. However, in several flight tests, the roll rate was seen to build up due to the dihedral effect and, without wing twist or ailerons, could not be compensated. This led to a divergent lateral-directional behavior despite local stability. Figure 17 shows the time histories for the case where the lateral

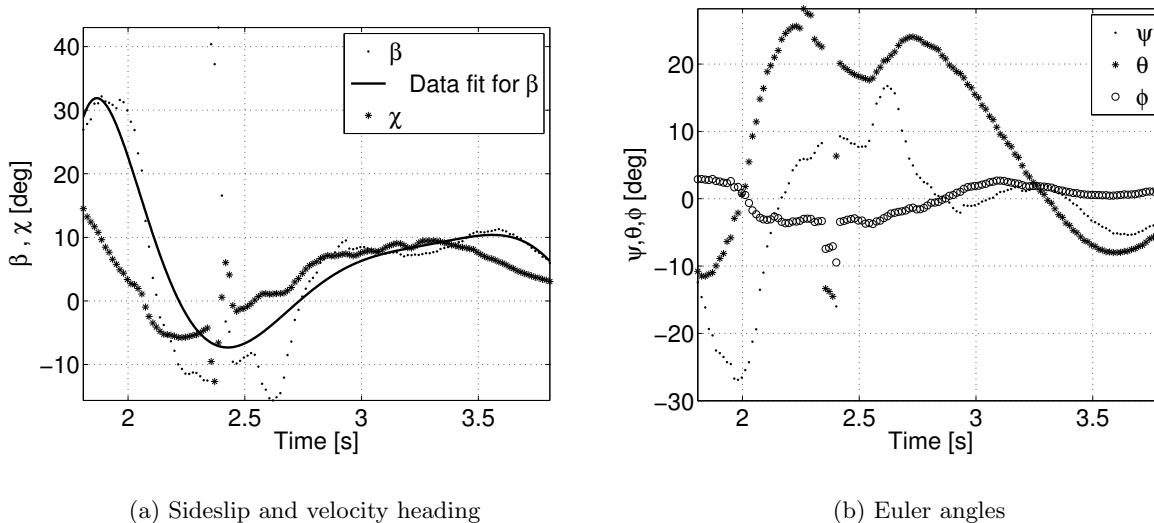


Figure 17: Experimental results showing the sideslip, velocity heading and the Euler angles measured during a yaw control test of the aircraft with a vertical tail. Parameters appear to be regulating during the short experiment

dynamics were seen to be stable. A zero heading angle was commanded. The heading angle as well as sideslip converge to small values. However, the transient response does not vanish within the limited flight duration. Nevertheless, the yaw rate slows significantly by the end of the flight indicating good closed loop stability characteristics. Lateral control of a tailless configuration is under experimental investigation.

9.6 Flight Path Control for Perching

An effective flight path controller is necessary for a successful perching maneuver. The aircraft must be able to track the desired flight path in order to arrive at a spatial target with an acceptable flight speed and height. The PID controller gains on the angle of attack controller were tuned to ensure sound tracking characteristics across a range of flight path angles. The flight path angle itself, as explained in section 9.3, is controlled using the wing dihedral angles.

9.7 Perching

9.7.1 Bioinspiration

Figure 18 shows some snapshots of an owl executing a perching maneuver, extracted from a reputed BBC documentary called the Life of Birds, and the clip was processed in Matlab. The longitudinal flight parameters, the flight path angle γ , the body axis pitch angle θ , and the angle of attack α , were extracted by making two assumptions: (a) the depth calibration was assumed to be unchanged, and (b) the local ground level was assumed to be approximately horizontal. These flight parameters have been plotted in Fig. 19. The perching maneuver is seen to consist of two phases: a gliding phase to bring the aircraft to a suitable position with respect to the landing spot, followed by a



Figure 18: Snapshots showing an owl in various stages of a perching maneuver, from BBC’s Life of Birds. The video was processed using Matlab.

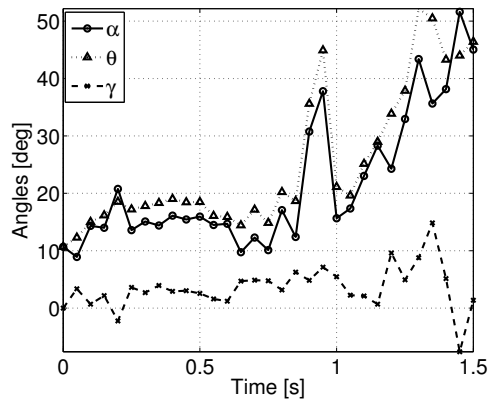


Figure 19: Angle of attack, flight path angle and pitch angle measurements from the BBC video of a perching owl. The maneuver was completed at $t = 1.5$ s.

rapid pitch up (usually to a post-stall angle of attack) which leads to an instantaneous climb and a rapid deceleration. Interestingly enough, an identical profile is obtained if the perching maneuver is designed by optimization [17, 18]: in particular, the elevator switched between two values, one corresponding to a low- α flight and the other being the saturation value of the elevator deflection which produced the desired post-stall angle of attack.

9.7.2 Experimental Demonstration of a Perching Maneuver

In conjunction with the guidance controller, a perching maneuver is executed as follows. An appropriate altitude is chosen such that a perching command is sent when the aircraft crosses it. This value was chosen to accommodate the actuation time delays for the wing dihedral as well as the elevator. Until this point, the angle of attack and flight path angle controllers described in Sec. 9.1 were used actively. Once the aircraft reaches the prescribed altitude, zero dihedral and maximum pitch-up elevator angles are commanded. These signals are held until touch-down. Figure 20 shows the perching signal sent at the 0.6 s mark. The angle of attack builds up to 30 deg, causing the speed to reduce, and the aircraft climbs momentarily. Flight speed is halved within 1 s to 3 m/s. After a brief ascent, the MAV lands at a low angle of attack. It is interesting to note that the final speed has reduced substantially even without using wing twist. Addition of wing twist would not only enable a further reduction in the final speed, but also provide for better

roll and yaw control during the approach.

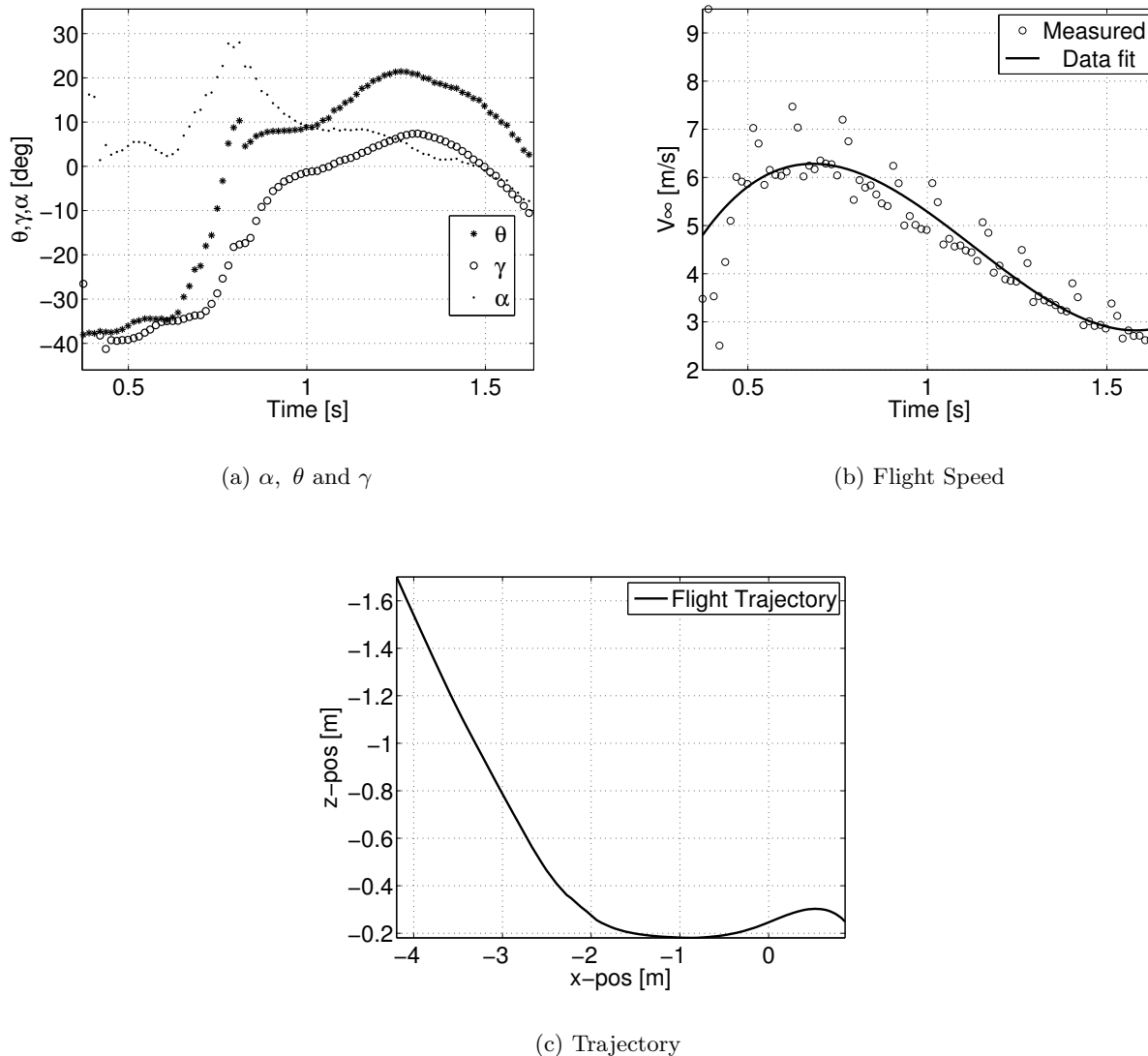


Figure 20: Flight parameters during a perching attempt that was triggered at 1.5m above the ground

9.8 Use of Trailing Edge Flaps for Mitigating Control Effectiveness Problems

Recall that the sign of the effectiveness depends on the sign $(x_a C_L/c + C_{m,ac})$, where x_a/c is the non-dimensional distance between the center of gravity and the quarter-chord line. Furthermore, $C_{m,ac} < 0$, and therefore, at small angles of attack, the control effectiveness is negative and it is positive at higher angles of attack. For an intermediate range of angles of attack, the sign depends on the angular rates as well.

In [26], it was shown that one way to get around this problem is to use trailing edge (TE) flaps.

TE flap deflection leads to a greater increase in C_L as compared to the reduction in $C_{m,ac}$. It is of interest to find the flap deflection, as a function of α , which will guarantee a certain positive control effectiveness. Suppose the desired value is 0.025 (see [26] for details). Then, for the aircraft considered in this paper, it follows that

$$\begin{aligned} \frac{C_L}{4} + C_{m,ac} + 0.72\delta_f &= 0.025, \quad (\text{where } \delta_f \text{ is the flap deflection}) \\ \therefore 0.07 + 0.5\alpha - 0.1311 + 0.72\delta_f &= 0.025 \implies \delta_f = 0.12 - 0.69\alpha \end{aligned} \quad (40)$$

The benefit of a uniformly positive control effectiveness, however, comes at a price: the aircraft is forced to fly in a high-lift, high drag configuration across the flight envelope. This necessarily means that the aircraft will fly slower than normal. However, note that the flight path angle can still be controlled effectively using symmetric dihedral deflection. Experimental results which validate this concept, and demonstrate its effectiveness in a successful perching maneuver, are reported in [26]. Figure 21 shows the flight parameters measured during a recently conducted set of perching experiments, while Fig. 22 shows a collection of snapshots depicting the perching maneuver.

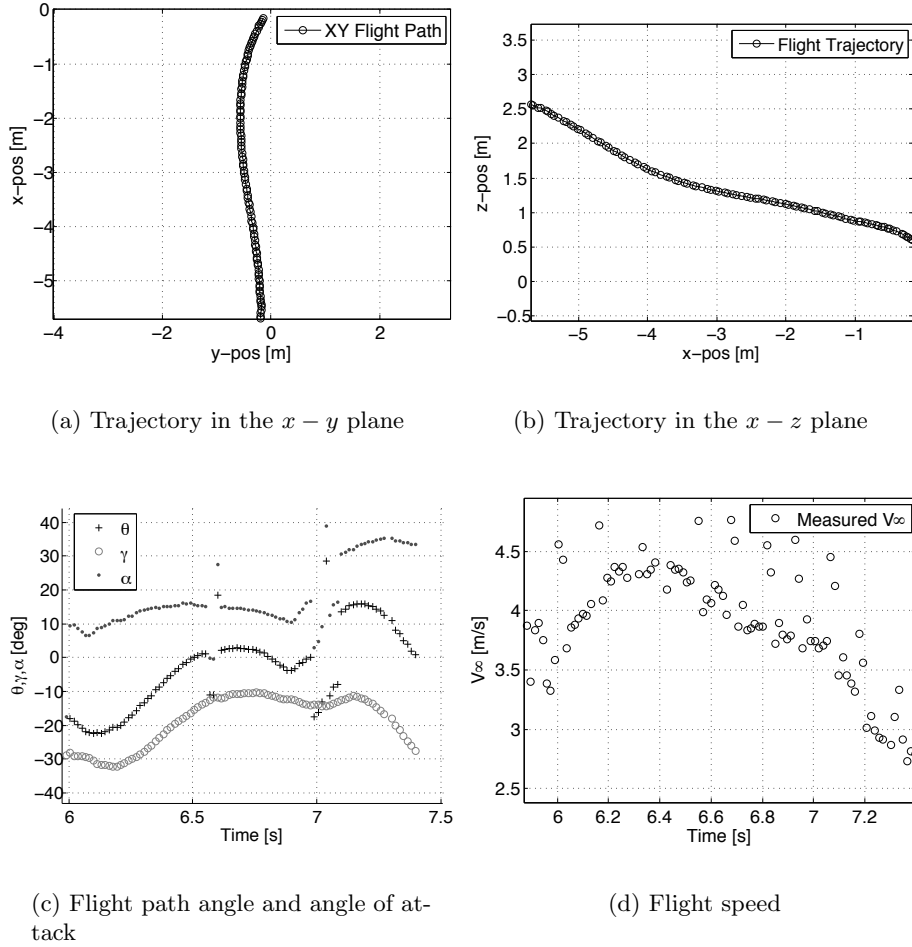


Figure 21: Flight parameters measured during a recent perching experiment.



Figure 22: Snapshots of a perching maneuver.

10 PDE Boundary Control of Flexible Wings

The motivation for considering the problem of boundary control of beams comes from the problem of controlling flexible wings for agile aircraft maneuvers. Let $\theta(t, y)$ denote the twist profile of the wing, and let $\xi(t, y)$ denote the bending displacement as a function of time and the spanwise coordinate y . The control objective is to ensure that

$$\lim_{t \rightarrow \infty} \left(\int_0^L \theta(t, y) dy - H(t) \right) = 0 \quad (\text{net lift, or}) \quad (41)$$

$$\lim_{t \rightarrow \infty} \left(\int_0^L y \theta(t, y) dy - H_l(t) \right) = 0 \quad (\text{net rolling moment, and}) \quad (42)$$

$$\lim_{t \rightarrow \infty} \left(\int_0^L \xi_y(t, y) dy - R(t) \right) = \lim_{t \rightarrow \infty} (\xi(t, L) - R(t)) = 0 \quad (\text{bending displacement of the tip}), \quad (43)$$

where $H(t)$, $H_l(t)$ and $R(t)$ are sufficiently smooth time-varying signals. Although we state asymptotic convergence as the objective, we will prove exponential convergence to a uniform ultimate bound. The term $\int_0^L \xi_y(t, y) dy = \xi(L)$ is a measure of the effective wing dihedral which is a key yaw control parameter [62], and it measures the amount of side (y -) force produced by the wing which, in turn, produces a yawing moment on the aircraft.

Remark: An important question that concerns systems described by PDEs is that of well-posedness. Well-posedness of the closed loop systems considered here can be shown by proving that the input-output map of the system is bounded [82, 11]. For the twisting dynamics actuated by root control, this is achieved by designing the control to map the system onto well-posed and exponentially stable dynamics. For twisting dynamics actuated at the wing tip, the input-output map is actually a finite order ODE, and its well-posedness follows from the standard existence and uniqueness theorems for ODEs. Finally, the well-posedness of the closed loop bending dynamics can be shown using a transfer function approach [11].

10.1 Boundary Control of Twisting Motion: Root Control

PDE backstepping is used for designing a boundary control law for wing twisting dynamics.

Backstepping is carried out in two steps: (a) the target dynamics are identified, and (b) a backstepping (Volterra) transformation converts the system dynamics (in this case, the error dynamics) into the target dynamics and the control signal $u(t)$ is obtained in the process. The method described by Krstic and Smyshlyaev [42] is used here. Let $\tilde{\theta}$ denote the error between the system state and the desired steady state value, i.e., $\tilde{\theta} = \theta - \theta_d$.

Next, consider the target dynamics described by the PDE

$$\begin{aligned} v_{tt} - bv_{t yy} - av_{yy} &= (M - ap)v - bpv_t, \\ v(t, 0) = v_y(t, L) &= 0 \end{aligned} \quad (44)$$

Using the method of separation of variables, it is easy to check that the eigenvalues of this system are the solutions of

$$\begin{aligned} \lambda^2 + b(\nu^2 + p)\lambda + (a(\nu^2 + p) - M) &= 0 \\ \text{where } \nu &= \frac{2n+1}{2} \frac{\pi}{L}, \quad n = 0, 1, 2, \dots \end{aligned} \quad (45)$$

The target dynamics are stable if and only if the control design parameter, p , satisfies

$$p > \max \left(\frac{M}{a} - \frac{\pi^2}{4L^2}, -\frac{\pi^2}{4L^2} \right) \quad (46)$$

A dummy spatial variable x is introduced and the Volterra transformation between $\tilde{\theta}$ (the error between the actual dynamics and the desired steady state in equation (44)) and v (the target dynamics for the error state) is given by

$$v(t, y) = \tilde{\theta}(t, y) - \int_L^y k(y, x) \tilde{\theta}(t, x) dx \quad (47)$$

It is helpful to recall that the $\tilde{\theta}$ dynamics are

$$\tilde{\theta}_{tt} - b\tilde{\theta}_{t yy} - a\tilde{\theta}_{yy} = M\tilde{\theta}, \quad \tilde{\theta}(t, 0) = u(t), \quad \tilde{\theta}_y(t, L) = 0 \quad (48)$$

In order to solve for $k(x, y)$, substitute equations (47) and (48) into equation (44). Next, isolating the coefficients of v and v_t , the following Klein - Gordon PDE for $k(y, x)$ is derived [42]

$$\begin{aligned} k_{xx}(y, x) - k_{yy}(y, x) &= -pk(y, x) \\ k(y, y) &= \frac{p}{2}(L - y), \quad k_x(y, L) = 0 \end{aligned} \quad (49)$$

The control input is found from equation (47)

$$u(t) = \tilde{\theta}(t, 0) = - \int_0^L k(0, x) \tilde{\theta}(t, x) dx \quad (50)$$

The solution is given in terms of the modified Bessel function I_1 *:

$$k(y, x) = p(L - y) \frac{I_1(\sqrt{p((L - y)^2 - (L - x)^2)})}{\sqrt{p((L - y)^2 - (L - x)^2)}} \quad (51)$$

A few observations are worth noting here.

1. If the wing is reasonably stiff $\left(\frac{MI_p}{G\tilde{J}} = \frac{M}{a} < \frac{\pi^2}{4L^2}\right)$; i.e., $G\tilde{J} > 4L^2MI_p/\pi^2$, the system can be stabilized with $p = 0$, i.e., with no additional control input.
2. For stability, it is essential that $b > 0$, i.e., the Kelvin-Voigt damping coefficient is always positive. A negative damping could be introduced due to aerodynamics, but it can be compensated by the term bpv_t and wing flutter can be prevented. The compensation in damping imposes an additional constraint on p .
3. The controller in equation (50) requires that the twist angle at all points on the wing be known. This difficulty can be circumvented by designing a PDE-based observer [42] or, practically, using a series of distributed sensors and fitting their output with an *a priori* designed spline.
4. Damping and stiffness cannot be added independently. They are added in the ratio b/a .
5. Finally, the control law does not require that a , b or M be known for the purpose of regulation. We only need to know bounds on a and M to choose an appropriate value of the gain p .

The backstepping controller shown above is, strictly speaking, a stabilizing controller: it regulates $\theta(t, y) \rightarrow 0$. The problem of designing a tracking controller which achieves the objective in (41) needs further work. Consider the system realized via the coordinate transformation

$$w(t, y) = \int_L^y \theta(t, x) dx \quad (52)$$

Physically, $w(t, y)$ measures the lift generated by the outboard section of the wing starting at y and terminating at the wing tip. The lift produced at the wing tip is zero, which is physically correct. Note that $\theta_y(t, L) = 0$ at the free end $y = L$. Hence, it follows that

$$\begin{aligned} w_{tt}(t, y) &= \int_L^y \theta_{tt}(t, x) dx = \int_L^y (b\theta_{txx}(t, x) + a\theta_{xx}(t, x) + M\theta(t, x)) dx \\ &= b\theta_{ty}(t, y) + a\theta_y(t, y) + Mw(t, y) = bw_{tyy}(t, y) + aw_{yy}(t, y) + Mw(t, y) \end{aligned} \quad (53)$$

Thus, the dynamics of w are described by the PDE

$$w_{tt} - bw_{tyy} - aw_{yy} = Mw, \quad w(t, L) = 0, \quad w_y(t, 0) = u(t), \quad (54)$$

where $u(t)$ is the control signal (θ_R), and recall that $a = G\tilde{J}/I_p$ and $b = \eta a$. Furthermore, we defined M so that $M\theta = -x_a c F_b / I_p$, where F_b is a linear function of θ . Note that $w_y(t, y) = \theta(t, y)$. Recall that the control objective is to ensure that $\lim_{t \rightarrow \infty} (\int_0^L \theta dy - H(t)) = 0$ (see equation (41)). The

*A modified Bessel function, $I_n(y)$, satisfies $y^2 I_n''(y) + y I_n'(y) - (y^2 + n^2) I_n(y) = 0$.

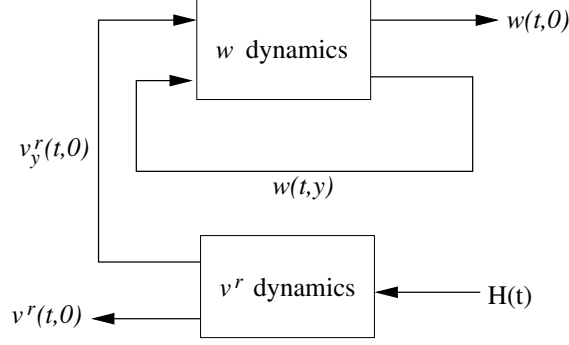


Figure 23: Block diagram showing the tracking controller for twist (θ) dynamics. This structure is identical to the classic strict feedback structure for systems described by ODEs [41].

control objective is now recast to ensuring that $\lim_{t \rightarrow \infty} (w(t, 0) + H(t)) = 0$, i.e., $\lim_{t \rightarrow \infty} w(t, 0) = -H(t)$.

The method for designing a tracking controller involves the following three steps:

1. Obtain a backstepping transformation $w \mapsto v$, although the boundary conditions are changed to match the tracking requirement,
2. Identify the boundary conditions for tracking and
3. Derive a motion planning-based design for the boundary conditions of the v dynamics.

The details of this method can be found in [63]. The control design procedure has been illustrated via a block diagram in Fig. 23.

10.2 Boundary Control of Twisting Motion: Wing Tip Control

As in the previous section, one can design a backstepping controller for the case where a control moment is applied to the free end ($y = L$) of the wing while the other end ($y = 0$) is clamped. In fact, the procedure in both cases is identical, although the final expressions for the control law differ slightly. Alternately, in case of MAVs, one may do without a stabilizing controller. The “tracking half” of the controller (without the stabilizing backstepping controller) may be designed using the output measurements. This method is useful for adaptive designs as well. We consider the wing model

$$\theta_{tt} - b\theta_{tyy} - a\theta_{yy} = M\theta, \quad \theta(t, 0) = 0, \quad \theta_y(t, L) = u(t) \quad (55)$$

where the control input is a moment applied at the wing tip. The control objective is to ensure that

$$\lim_{t \rightarrow \infty} \left(\int_0^L \theta(t, y) dy - H(t) \right) = 0 \quad (56)$$

Let $e(t) = \int_0^L \theta(t, y) dy - H(t)$ denote the error which needs to be regulated. Then,

$$\begin{aligned}
\ddot{e} &= \int_0^L \theta_{tt}(t, y) dy - \ddot{H}(t) \\
&= \int_0^L (a\theta_{yy} + b\theta_{tyy} + M\theta) dy - \ddot{H}(t) \\
&= a\theta_y(L) - a\theta_y(0) + b\theta_{ty}(L) - b\theta_{ty}(0) + Me(t) - \ddot{H}(t) + MH(t) \\
&= b\dot{u}(t) + au(t) - a\theta_y(0) - b\theta_{ty}(0) + Me(t) - \ddot{H}(t) + MH(t)
\end{aligned} \tag{57}$$

A dynamic controller of the form

$$b\dot{u}(t) + au(t) = \ddot{H}(t) - MH(t) - (M + k)e(t) - k_c\dot{e}(t) + a\theta_y(0) + b\theta_{ty}(0) \tag{58}$$

renders the system into the spring-mass form

$$\ddot{e}(t) + k_c\dot{e}(t) + ke(t) = 0. \tag{59}$$

The control law in equation (58) suggests that θ need not be monitored or measured at all locations on the wing. Instead, only $\theta_y(0)$ needs to be measured or estimated. The reference signal $H(t)$ is known. It may be difficult to inject damping because $\dot{e}(t)$ is the rate of change of the lift and in practice, would require differentiating noisy acceleration signals.

Another interesting observation is that although the PDE system had an infinite relative degree when the root twist was chosen as the control input, the relative degree is 2 when twisting moment at the wing tip is considered as the input. This facilitates the control law design in this section considerably. The control law design described in this section lends itself readily to adaptation should a and/or M be unknown.

Consider the dynamics in equation (55) with the objective in equation (56) and suppose that M is unknown. The control law in (58) is modified so that

$$b\dot{u}(t) + au(t) = \ddot{H}(t) - \hat{M}(t)(H(t) + e(t)) - ke(t) - k_c\dot{e}(t) + a\theta_y(0) + b\theta_{ty}(0) \tag{60}$$

where $\hat{M}(t)$ is the estimated value of M . The error dynamics are described by the ODE

$$\ddot{e}(t) + k_c\dot{e}(t) + ke(t) = -\tilde{M}(t)(H(t) + e(t)), \tag{61}$$

where $\tilde{M}(t) = \hat{M}(t) - M(t)$. The adaptive law for $\hat{M}(t)$

$$\dot{\hat{M}}(t) = \gamma \text{Proj} \left(\hat{M}(t), x^T P \begin{bmatrix} 0 \\ 1 \end{bmatrix} (e(t) + H) \right) \tag{62}$$

ensures that the error $e(t)$ remains bounded on the order $\mathcal{O}(1/\gamma)$, so that the adaptive gain can be chosen to match the tracking accuracy requirements. Although a and b were assumed to be known, the aforementioned analysis can be repeated to accommodate an unknown a and b as well.

10.2.1 Tracking and Stability

The problems of tracking and stabilization are distinct because the PDE system is infinite dimensional. Nevertheless, a tracking controller improves stability as described presently. The best way to understand the influence of a tracking controller is to set $H = 0$. Make a coordinate transformation $w(t, y) = \int_L^y \theta(t, y) dy$ so that achieving $H = 0$ is equivalent to achieving $w(0) \triangleq w(t, 0) = 0$. It follows that the transformed dynamics, with $H = 0$ ensured by the tracking algorithm, are given by

$$w_{tt}(t, y) - bw_{t yy}(t, y) - aw_{yy}(t, y) = Mw(t, y) - bw_{t yy}(t, 0) - aw_{t yy}(t, 0), \quad w(L) = w(0) = 0, \quad w'(0) = 0 \quad (63)$$

The third boundary condition is not entirely independent. Let $w(t, y) = \eta(t)\phi(y)$. Then, we get

$$\frac{\ddot{\eta}(t) - M\eta(t)}{b\dot{\eta}(t) + a\eta(t)} = \frac{\phi''(y) - \phi''(0)}{\phi(y)} = -\lambda^2, \quad (64)$$

where λ is a constant. It follows that the condition for stability is $M/a < \lambda^2$. The differential equation for $\phi(y)$ can be solved to get

$$\phi(y) = A \sin(\lambda y) + B \cos(\lambda y) + \phi''(0)/\lambda^2 \quad (65)$$

The boundary conditions $\phi(0) = \phi'(0) = 0$ lead to $\phi(y) = B(\cos(\lambda y) - 1)$. Finally,

$$\phi(L) = 0 \implies \lambda = 2n\pi/L, \quad \because \phi(L) = 0, \quad n = 1, 2, \dots \quad (66)$$

Had we not imposed the condition $H(0) = 0$, we would have obtained $M/a < \pi^2/(4L^2)$ as the condition for stability. Since the condition for open loop stability is given by $M/a < \lambda^2 = 4\pi^2/L^2$, it follows that the stability margin improves by a factor of sixteen *using only the tracking controller*, although, it does not stabilize the wing for all values of M and a as backstepping does. In principle, the tracking controller converts the wing from a cantilever beam to a clamped-clamped beam. In practice, this translates to the ability to increase the wing flexibility by an order of magnitude, or increase the wing divergence speed four-fold. This is shown in Fig. 24.

10.3 Control of Rolling Moment

An abstract measure of the rolling moment is $\int_0^L y\theta(t, y)dy$, defined in equation (42). Let $e_l(t, y) = \int_0^L y\theta(t, y)dy - H_l(t)$, where $H_l(t)$ denotes the reference value of the rolling moment to be tracked, and $e_l(t)$ is the tracking error. Differentiate $e_l(t)$ twice with respect to time:

$$\begin{aligned} \ddot{e}_l(t) &= \int_0^L y\theta_{tt}(t, y)dy - \ddot{H}_l(t) \\ &= \int_0^L y(b\theta_{t yy}(t, y) + a\theta_{yy}(t, y))dy + M \int_0^L y\theta(t, y)dy - \ddot{H}_l(t) \\ &= L(b\theta_{ty}(t, L) + a\theta_y(t, L)) - b(\theta_t(t, L) - \theta_t(t, 0)) - a(\theta(t, L) - \theta(t, 0)) + Me_l(t) + MH_l(t) - \ddot{H}_l(t) \end{aligned} \quad (67)$$

An interesting observation is that $e_l(t)$ has a relative degree of 2 with respect to $\theta_y(L)$ (tip control) as well as $\theta(0)$ (root control). In particular, it means that a considerably simpler controller than

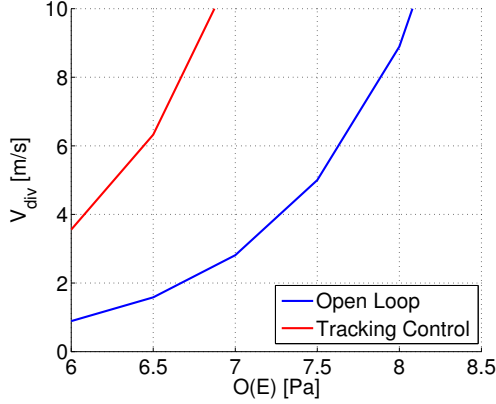


Figure 24: Torsional divergence speed as a function of the Young’s modulus of the wing. The blue curve is the open loop divergence speed, while the red curve is the divergence speed after adding the tip-based twist controller.

the backstepping controller, on the lines of the adaptive controller in the previous section, can be implemented for a root-based actuator. Indeed, in aircraft, the lift is controlled using the horizontal tail, while wing-based flaps (ailerons and spoilers) are used primarily for roll control.

10.4 Root Control for Wing Bending

The bending PDE can be written as

$$\begin{aligned} \tilde{m}\xi_{tt} + \eta EI_b \xi_{tyyyy} + EI_b \xi_{yyyy} &= F_n(t, y, \xi_t, \theta, \theta_{tt}), \\ \xi(t, 0) = \xi_{yy}(t, L) = \xi_{yyy}(t, L) &= 0, \quad \xi_y(t, 0) = u(t), \end{aligned} \quad (68)$$

where the control input $u(t) = \delta_R(t)$ is designed to ensure that $\xi(t, L) = R(t)$ in (43). The acceleration term corresponding to $\tilde{m}x_e c \ddot{\theta}$ (due to twist) has been moved to the right hand side and merged into F_b , so that $F_n = F_b + \tilde{m}x_e c \ddot{\theta}$. The interesting point about equation (68) is that the right hand side is independent of ξ , and θ is an average value obtained from the faster twist dynamics. Therefore, unlike the twisting dynamics, the onset of instability in the bending dynamics will correspond to the damping becoming negative.

Bending dynamics are usually stable, in that there is no direct aerodynamic driver of instability as there is in the case of torsion. If the beam dynamics are unstable PDE backstepping can be used to inject damping into the system. A procedure for backstepping, based on a transformation of the bending dynamics into the Schrödinger equation, has been detailed in Krstic and Smyshlyaev (See Ch. 8 of Ref. [42]). A tracking controller can be added on top of the backstepping controller for tracking. We focus on a motion planning-based design for a tracking controller. However, note that $F(t, y)$ is usually not measurable in practice, although one may estimate its spatial profile from the wing geometry [49].

In this section, we design an observer-based controller to facilitate a motion-planning-based tracking controller for bending. The perturbation observer does not predict the system states. It uses projection-based adaptation to estimate $F(t, y)$ which would be unknown in practical situations. The perturbation observer is split into a “particular” and a “homogeneous” component (the

notions will be made more precise in this section). In particular, the homogeneous component is stable and not driven directly by external feedback. Thus, it is simpler to design a control law for it. The same control signal is sent to the actual system, whose states then converge exponentially to a bounded envelope around the observer states.

Let $F(t, y) = W(t)^T \phi_b(y) + \sigma(t)$ where $W(t)$ and $\sigma(t)$ are unknown and bounded with known bounds. The set of functions, $\phi_b(y)$, can be chosen to get a satisfactory bound on σ , and using a knowledge of the wing geometry [49].

The perturbation observer can be designed as a sum of two states, $\hat{\xi} = \hat{\xi}_h + \hat{\xi}_p$, where the dynamics of the two states $\hat{\xi}_h$ and $\hat{\xi}_p$ are described by the following PDEs:

$$\begin{aligned} \hat{\xi}_{p,tt}(t, y) + b_b \hat{\xi}_{p,tyyyy}(t, y) + a_b \hat{\xi}_{p,yyyy}(t, y) &= -b_b p \tilde{\xi}_{p,t}(t, y) - a_b p \tilde{\xi}_p(t, y) + \hat{W}(t)^T \phi_b(y) + \hat{\sigma}(t), \\ \hat{\xi}_{p,yy}(L) = \hat{\xi}_{p,yyy}(L) = \hat{\xi}_p(0) = \hat{\xi}_{p,y}(0) &= 0 \end{aligned} \quad (69)$$

for the particular component, where $\tilde{\xi}_p = \hat{\xi}_p - \xi$, and

$$\begin{aligned} \hat{\xi}_{h,tt} + b_b \hat{\xi}_{h,tyyyy} + a_b \hat{\xi}_{h,yyyy} &= -b_b p \hat{\xi}_{h,t} - a_b p \hat{\xi}_h, \\ \hat{\xi}_{h,yy}(L) = \hat{\xi}_{h,yyy}(L) = \hat{\xi}_h(0) = 0, \quad \hat{\xi}_{h,y}(0) &= u(t) \end{aligned} \quad (70)$$

for the homogeneous component. Here $\tilde{\xi} = \hat{\xi} - \xi$ and $p > 0$ is chosen to ensure desirable convergence properties. Projection-based adaptive law for $\hat{W}(t)$ and $\hat{\sigma}(t)$,

$$\begin{aligned} \dot{\hat{W}}(t) &= \gamma_a \text{Proj} \left(\hat{W}(t), - \int_0^L (\tilde{\xi}_t + \delta \tilde{\xi}) \phi_b(y) dy \right) \\ \dot{\hat{\sigma}}(t) &= \gamma_a \text{Proj} \left(\hat{\sigma}(t), - \int_0^L (\tilde{\xi}_t + \delta \tilde{\xi}) dy \right) \end{aligned} \quad (71)$$

lead to error dynamics between the perturbation observer and the actual system that are stable, and in fact, globally uniformly bounded.

This observer can be used in the motion planning algorithm to ensure that the wing tip tracks the desired displacement profile. The motion planning is performed in practice on the homogeneous half of the observer. Note that the homogeneous half is a stable system and its dynamics are not influenced in any way by ξ or $\hat{\xi}_p$. The details of motion planning are given in [63]. Figure 25 is a block diagram of the perturbation observer. Notice that the reference input, $R(t)$ from (43), enters only the homogeneous component of the perturbation observer, while the feedback from the actual system only enters the particular component.

10.5 Simulations

Simulations are carried out in Matlab using a Galerkin-based approach to convert the PDE system into ODEs. The Galerkin truncation is not used as a basis for control law design, so no danger of a “spillover instability” arises. Figure 26 demonstrates the regulation of twist dynamics using the backstepping controller derived in equation (50), with the transformation in equations (47) and (49). The value of M/a was set to 8, where $a = G\tilde{J}/I_p$. A value of $p = 4$ yielded an unstable response, while the response was stable for $p = 8$. Recall the following condition for stability with $L = 1$: $p > M/a - \pi^2/4 \approx 2.53$. The backstepping controller works even when $M(y) = M(1 - y^2)$ is used (to mimic an elliptical lift distribution over the wing) instead of a constant $M(y) \equiv M$.

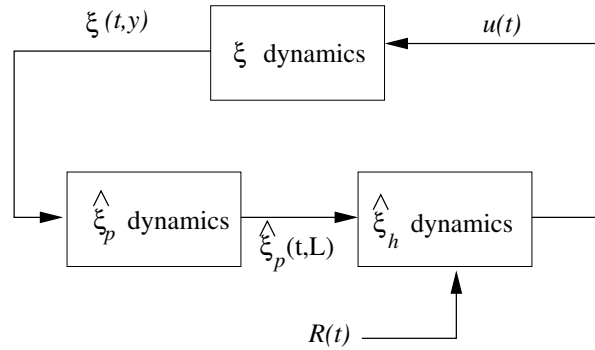
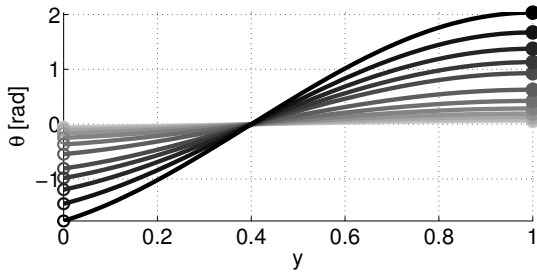
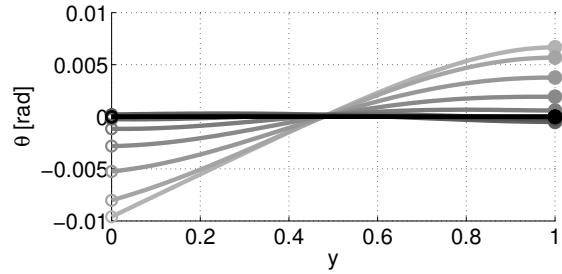


Figure 25: Block diagram for the perturbation observer coupled to the system dynamics. The control signal, $u(t)$, is generated from motion planning, while $R(t)$ is the desired reference signal from (43).



(a) Unstable response with $p = 4$



(b) Stable response with $p = 8$ for spatially-varying $M(y)$

Figure 26: Regulation of the twist dynamics using the backstepping controller in equation (50), with the transformation in equations (47) and (49). The plots were obtained for $M/a = 8$, while p was increased to ensure stability. Each plot is a collection of snapshots, where the lines get darker with time.

The backstepping controller can be added on top of a tracking controller.

Figure 27 shows the simulation of a wing actuated by tip control. The value of M/a was chosen so that stability is assured without the need for a dedicated stabilizing controller. The first plot was obtained for a system where the aerodynamics were assumed to be linear but unknown. The second plot was obtained for the case where the aerodynamics were additionally spatially varying and rendered the open loop dynamics unstable. The time histories of the tracking error $e(t)$, and the control signal $u(t)$, for the second case are plotted in Fig. 28. In both cases, the twist amplitude converges to the steady state value with satisfactory transients. The error metric equation (41) is also seen to be very small. Note that the control signal, obtained from Eq. (60), is almost noise-free. This is because the dynamic controller acts like a low pass filter and ensures that noisy terms arising from the high gain terms on the right hand side of Eq. (60) are filtered out.

Finally, figure fig:BendSims shows the time histories tip displacement for a wing whose bending motion is actuated by a root-based actuator. The dashed lines show the reference signal for wing tip displacement, while blue lines show the actual displacement of the wing tip. The first simulation was obtained for the case where $F(t, y)$ was set to zero, while the second plot was obtained for a time varying $F(t, y)$. The motion planning algorithm used a seventh order polynomial in the spatial variable y . In both cases, the tracking is seen to be satisfactory and noise free.

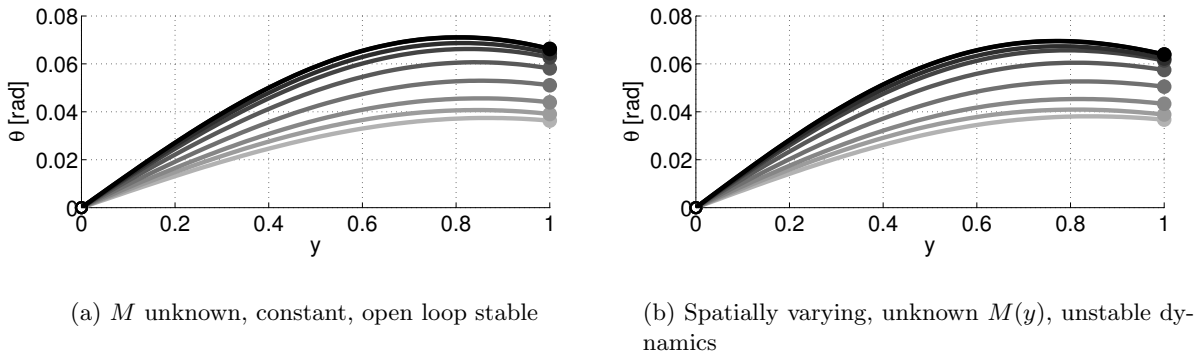
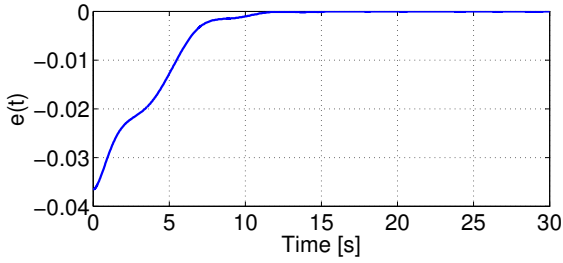


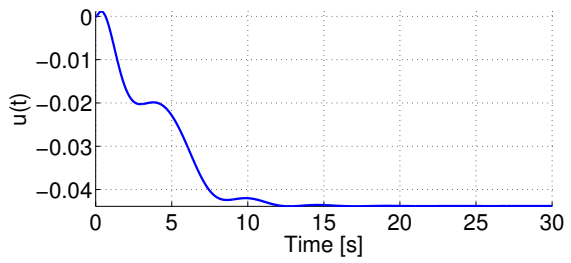
Figure 27: Twist profile of the wing as a function of time when the the adaptive controller in equation (60) is applied at the wing tip. Three cases have been examined here, with $\int_0^L \theta(t, y) dy = 0.05$ as the desired output. Each plot shows appropriately chosen snapshots, with lines getting darker with time.

10.6 Section Summary

Tools from PDE boundary control show considerable promise for the efficient control of flexible structures in general, and of flexible wings in particular. The key contributions of this work were: (a) the design of a PDE backstepping based tracking controller for wing twist, (b) the finite degree problem formulation for wing twist control using a tip-based actuator, (c) the study of the enhancement in stability due to a tracking controller, and (d) the design of a perturbation observer based controller for wing bending. It is safe to claim that every contribution listed above leads to a related open problem in PDE control. The most important open problem is the design of a coupled twist-bending controller.



(a) Time history of $e(t)$



(b) Time history of $u(t)$

Figure 28: Time histories of the error $e(t)$ and the control signal $u(t)$ for the case of spatially varying, unknown $M(y)$ with unstable open loop dynamics.

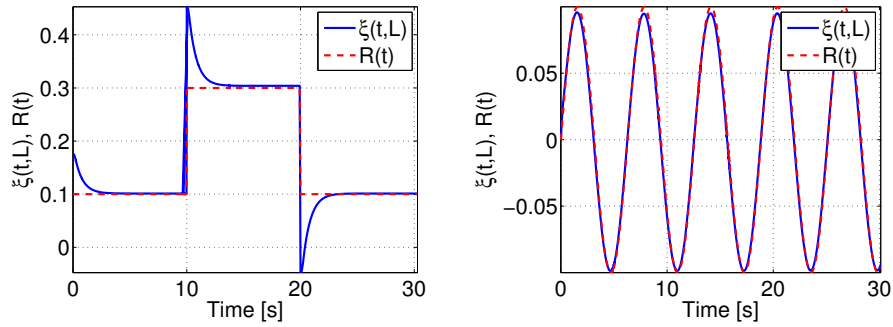


Figure 29: Time history of the wing tip displacement for two classes of reference signals: a pulse and a sine wave. The first two plots were obtained with the right hand side set to zero, while the third plot was obtained for a time varying $F(t, y)$ in equation (68).

11 Conclusions

The objective of this work was to study the unique dynamics and control characteristics of tailless MAV equipped with articulated wings. We studied the performance and stability using a combination of literal approximations, numerical trim and stability computations, and experiments. We showed that the dihedral angle of the wing can be varied symmetrically to obtain an additional degree of freedom, namely the ability to change flight path angle independently of the flight speed. We demonstrated that asymmetric dihedral settings can be used to perform rapid turns and control the sideslip. From the standpoint of control, the most important observation was the discovery of maneuver-dependent control effectiveness reversal.

Bat-like flight is a challenging problem that cannot be solved via averaging or with traditional tail-derived stability. We have demonstrated the ability to stabilize and control longitudinal motions via CPGs with the RoboBat. As expected, the top-level controllers are of low dimension and can be made very simple, because most of the hard work is done by the CPGs. Given the extent of mechanical coupling in the design, it is remarkable that such control was immediately as effective

as it was. Further work can still be done to create a pattern generator layer so to optimize the output waveforms. Additionally, we expect to quantify the forces and moments actually produced via the aerodynamic model, so that we can make better predictions for a free-flying robotic bat.

As mechanical design of actuators develops, we expect robotic fliers in free flight to be able to utilize the key feature of phase synchronization and control of phase differences in stability and control of body motions. The major problem of identifying a method of proving such stability analytically is still open. However, this work has demonstrated the successful CPG-based flight control result experimentally by using the RoboBat. Since this CPG controller design also features rapid inhibition of oscillation, it leads to the important problem of gliding flight and maneuvers while gliding.

The performance and stability characteristics of a flexible aircraft were compared with those of a rigid aircraft, assuming that the wings of the flexible aircraft were statically deformed. We presented a metric called the effective dihedral for flexible wings which allows the results from the analysis of a rigid aircraft to be extended to flexible aircraft. Moreover, it allows us to identify the extent to which conclusions regarding the performance of rigid aircraft apply to a flexible-winged aircraft. Although we did not observe any difference in stability characteristics, there were interesting differences in the turn performance. Although wing flexibility was shown to help reduce the sideslip significantly, it was also shown to reduce the maximum attainable turn rate under a zero-sideslip constraint compared to a rigid aircraft with identical elevator settings. This was attributed to the reduction in flight speed due to wing twist.

The open loop characteristics of a tailless MAV were tested experimentally to verify the analytical predictions. Control laws motivated by dynamic inversion were designed and tested on an experimental aircraft. The experiments exposed the impediments that arise due to the reversal of control effectiveness. At the same time, they demonstrated the ability of articulated wings to aid steep descents and perching maneuvers, as well as their capability for yaw control.

Finally, we designed PDE-based control laws for controlling the deformation of a flexible wing to achieve a net aerodynamic force or moment. We considered cases where the actuators were based at the wing root as well as the tip. PDE backstepping-based control laws were developed for controlling wing twist using root-based actuators. We showed that a tracking controller could bring about a significant improvement in the stability margin of the wing dynamics, measured by the critical flight speed or elastic modulus for the onset of instability. We showed that the time scale separation between the bending and twisting dynamics depends primarily on the aspect ratio of the wing and the flight speed. We designed a controller for bending independently of the one for wing twist. The controller designed for bending used a novel idea based on splitting a perturbation-observer into two parts, one of which accommodated the external forces and the other which accommodated the boundary control. Thereafter, motion planning was used to design the boundary controller, with the understanding that it could be added readily on top of a stabilizing controller if required.

References

- [1] N. Ananthkrishnan and S. Unnikrishnan, "Literal approximations to aircraft dynamic modes," *Journal of Guidance, Control and Dynamics*, vol. 24, no. 6, pp. 1196 – 1203, 2001.
- [2] A. Azuma, *The Biokinetics of Flying and Swimming*, 2nd ed. American Institute of Aeronautics and Astronautics, 2006.

- [3] N. Baghdadi, M. H. Lowenberg, and A. T. Isikveren, “Analysis of flexible aircraft dynamics using bifurcation methods,” *Journal of Guidance, Control and Dynamics*, vol. 34, no. 3, pp. 795 – 809, 2011.
- [4] M. J. Balas, “Feedback control of flexible systems,” *IEEE Transactions on Automatic Control*, vol. 23, no. 4, pp. 673 – 679, 1978.
- [5] S. Bieniawski and I. M. Kroo, “Flutter suppression using micro-trailing edge effectors,” in 44th *AIAA/ASME/ASCE/AHS Structures, Structural Dynamics, and Materials Conference*, 2003, AIAA 2003–1941.
- [6] R. L. Bisplinghoff, A. Holt, and R. L. Halfman, *Aeroelasticity*, 1st ed. Dover, Mineola, NY, 1996.
- [7] M. A. Bolender, “Rigid multi-body equations-of-motion for flapping wing mavs using Kanes equations,” in *Proc. AIAA Guidance, Navigation and Control Conference, Chicago, IL*, 2009, AIAA Paper 2009–6158.
- [8] P. Bourdin, A. Gatto, and M. Friswell, “Aircraft control via variable cant-angle winglets,” *Journal of Aircraft*, vol. 45, no. 2, pp. 414 – 423, 2008.
- [9] F. Bucci and I. Lasiecka, “Optimal boundary control with critical penalization for a PDE model of fluid-solid interactions,” *Calculus of Variations*, vol. 37, pp. 217 – 235, 2009.
- [10] A. Chakravarthy, A. A. Paranjape, and S.-J. Chung, “Control law design for perching an agile mav with articulated wings,” in *Proc. AIAA Atmospheric Flight Mechanics Conference, Toronto, ON, Canada*, 2010, AIAA Paper 2010–7934.
- [11] A. Cheng and K. Morris, “Well-posedness of boundary control systems,” *SIAM Journal of Control and Optimization*, vol. 42, no. 4, pp. 1244 – 1265, 2003.
- [12] P. D. Christofides and P. Daoutidis, “Feedback control of hyperbolic PDE systems,” *AIChE Journal*, vol. 42, no. 11, pp. 3063–3086, 1996.
- [13] ———, “Finite-dimensional control of parabolic PDE systems using approximate inertial manifolds,” in *Proceedings of the 36th IEEE Conference on Decision and Control*, 1997, pp. 1068–1073.
- [14] S.-J. Chung and M. Dorothy, “Neurobiologically inspired control of engineered flapping flight,” *Journal of Guidance, Control and Dynamics*, vol. 33, no. 2, pp. 440–453, 2010.
- [15] S.-J. Chung, M. Dorothy, and J. R. Stoner, “Neurobiologically inspired control of engineered flapping flight,” in *AIAA Infotech at Aerospace and Unmanned Unlimited Conference and Exhibit*, Seattle, WA, Apr. 2009, aIAA Paper 2009-1929.
- [16] S.-J. Chung and J.-J. E. Slotine, “Cooperative robot control and concurrent synchronization of lagrangian systems,” *IEEE Transactions on Robotics*, vol. 25, no. 3, pp. 686–700, 2009.
- [17] R. Cory and R. Tedrake, “Experiments in fixed-wing UAV perching,” in *Proc. AIAA Guidance, Navigation and Control Conference, Honolulu, HI*, 2008, AIAA Paper 2008–7256.

- [18] W. J. Crowther, “Perched landing and takeoff for fixed wing UAVs,” Tech. Rep., 2000.
- [19] R. F. Curtain and H. J. Zwart, *An Introduction to Infinite-Dimensional Linear Systems Theory*, ser. Texts in Applied Mathematics. Springer-Verlag, 1995, no. 21.
- [20] J. D. DeLaurier, “An aerodynamic model for flapping-wing flight,” *Aeronautical Journal*, vol. 97, no. 964, pp. 125 – 130, 1993.
- [21] X. Deng, L. Schenato, and S. S. Sastry, “Flapping flight for biomimetic robotic insects: Part II: Flight control design,” *IEEE Transactions on Robotics*, vol. 22, no. 4, pp. 789 – 803, 2006.
- [22] X. Deng, L. Schenato, W. C. Wu, and S. S. Sastry, “Flapping flight for biomimetic robotic insects: Part I-system modeling,” *IEEE Transactions on Robotics*, vol. 22, no. 4, pp. 776 – 788, 2006.
- [23] D. B. Doman, M. Oppenheimer, and D. Sigthorsson, “Wingbeat shape modulation for flapping-wing micro-air-vehicle control during hover,” *Journal of Guidance, Control and Dynamics*, vol. 33, no. 3, pp. 724 – 739, 2010.
- [24] D. B. Doman, C. P. Tang, and S. Regisford, “Modeling interactions between flexible flapping-wing spars, mechanisms, and drive motors,” *Journal of Guidance, Control and Dynamics*, vol. 34, no. 5, pp. 1457 – 1473, 2011.
- [25] M. Dorothy and S. Chung, “Methodological remarks on cpg-based control of flapping flight,” in *AIAA Atmospheric Flight Mechanics Conference*, Toronto, ON, Aug. 2010, aIAA Paper 2010-7634.
- [26] M. Dorothy, A. A. Paranjape, P. D. Kuang, and S.-J. Chung, *Towards Bio-inspired Robotic Aircraft: CPG-based Control of Autonomous Flapping and Gliding Flight*, ser. AIAA Progress in Aeronautics and Astronautics. American Institute of Aeronautics and Astronautics (AIAA), Reston, VA, 2012, to be published Spring 2012.
- [27] M. P. Fard and S. I. Sagatun, “Exponential stabilization of a transversely vibrating beam by boundary control via Lyapunov’s direct method,” *Journal of Dynamic Systems, Measurement, and Control*, vol. 123, pp. 195 – 200, 2001.
- [28] A. Gatto, P. Bourdin, and M. Friswell, “Experimental investigation into articulated winglet effects on flying wing surface pressure aerodynamics,” *Journal of Aircraft*, vol. 47, no. 5, pp. 1811 – 1816, 2010.
- [29] M. Goman and A. Khrabrov, “State-space representation of aerodynamic characteristics of an aircraft at high angles of attack,” *Journal of Aircraft*, vol. 31, no. 5, pp. 1109 – 1115, 1994.
- [30] M. G. Goman, G. I. Zagaynov, and A. V. Khramtsovsky, “Application of bifurcation theory to non-linear flight dynamics problems,” *Progress in Aerospace Sciences*, vol. 33, no. 9, pp. 539 – 586, 1997.
- [31] M. Hamamoto, Y. Ohta, K. Hara, and T. Hisada, “A fundamental study of wing actuation for a 6-in-wingspan flapping microaerial vehicle,” *IEEE Transactions on Robotics*, vol. 26, no. 2, pp. 244 – 255, 2010.

- [32] W. He, S. S. Ge, B. V. E. How, Y. S. Choo, and K. S. Hong, “Robust adaptive boundary control of a flexible marine riser with vessel dynamics,” *Automatica*, vol. 47, pp. 722 – 732, 2011.
- [33] F. Herrero-Carrón, F. B. Rodríguez, and P. Varona, “Bio-inspired design strategies for central pattern generator control in modular robotics,” *Bioinsp. Biomim.*, vol. 6, 2011.
- [34] D. H. Hodges and A. G. Pierce, *Introduction to Structural Dynamics and Aeroelasticity*, ser. Cambridge Aerospace Series. Cambridge University Press, 2002, no. 15.
- [35] N. Hovakimyan, E. Lavretsky, and A. Sasane, “Dynamic inversion for nonaffine-in-control systems via time-scale separation. Part I,” *Journal of Dynamical and Control Systems*, vol. 13, no. 4, pp. 451 – 465, 2007.
- [36] S. A. Hubbard, D. M. McFarland, L. A. Bergman, and A. F. Vakakis, “Targeted energy transfer between a model flexible wing and nonlinear energy sink,” *Journal of Aircraft*, vol. 47, no. 6, pp. 1918 – 1931, 2010.
- [37] W. Johnson, *Helicopter Theory*. Dover New York, 1980.
- [38] J. D. Keller, R. M. McKillip Jr, and S. Kim, “Aircraft flight envelope determination using upset detection and physical modeling methods,” in *Proc. AIAA Atmospheric Flight Mechanics Conference, Hilton Head, SC*, 2009, AIAA Paper 2009–6259.
- [39] J. D. Keller, R. M. McKillip Jr, and D. A. Wachspress, “Physical modeling of aircraft upsets for real-time simulation applications,” in *Proc. AIAA Atmospheric Flight Mechanics Conference, Honolulu, HI*, 2008, AIAA Paper 2008–6205.
- [40] M. Krstic, B.-Z. Guo, A. Balogh, and A. Smyshlyaev, “Control of a tip-force destabilized shear beam by observer-based boundary feedback,” *SIAM Journal of Control and Optimization*, vol. 47, no. 2, pp. 553 – 574, 2008.
- [41] M. Krstic, I. Kanellakopoulos, and P. V. Kokotovic, *Nonlinear and Adaptive Control Design*. Wiley, 1995.
- [42] M. Krstic and A. Smyshlyaev, *Boundary Control of PDEs: A Course on Backstepping Designs*. Advances in Design and Control, SIAM, 2008.
- [43] ———, *Adaptive Control of PDEs*. Princeton University Press, 2010.
- [44] P. D. Kuang, M. Dorothy, and S.-J. Chung, “Robobat: Dynamics and control of a robotic bat flapping flying testbed,” in *AIAA Infotech at Aerospace Conference, St. Louis, MO*, 2011, AIAA Paper 2011–1435.
- [45] A. M. Kuethe and C.-Y. Chow, *Foundations of Aerodynamics*, 4th ed. John Wiley, NY, 1986.
- [46] R. F. Larijani and J. D. DeLaurier, *A Nonlinear Aeroelastic Model for the Study of Flapping Wing Flight*. AIAA, 2001, pp. 399 – 428.

- [47] W. Lohmiller and J. J. E. Slotine, “Contraction analysis of nonlinear distributed systems,” *International Journal of Control*, vol. 78, no. 9, pp. 678 – 688, 2005.
- [48] M. Lowenberg, *Bifurcation and Continuation Method*. Springer-Verlag, 2002, pp. 88 – 106.
- [49] B. W. McCormick, *Aerodynamics, Aeronautics and Flight Mechanics*, 2nd ed. Wiley, 1994.
- [50] O. J. McMillan, R. G. Schwind, J. N. Nielsen, and M. F. E. Dillenius, “Rolling moments in a trailing vortex flow field,” NEAR TR 129, also NASA CR-151961, 1977.
- [51] L. Meirovitch and H. Baruh, “On the problem of observation spillover in self-adjoint distributed-parameter systems,” *Journal of Optimization and Applications*, vol. 39, no. 2, pp. 269 – 291, 1983.
- [52] L. Meirovitch and I. Tuzcu, “Unified theory for the dynamics and control of maneuvering flexible aircraft,” *AIAA Journal*, vol. 42, no. 4, pp. 714 – 727, 2004.
- [53] C. C. Merrett and H. H. Hilton, “Influences of starting transients, aerodynamic definitions and boundary conditions on elastic and viscoelastic wing and panel flutter,” *Mathematics in Engineering, Science and Aerospace*, vol. 2, no. 2, pp. 121 – 144, 2011.
- [54] T. J. Mueller, *Fixed and Flapping Wing Aerodynamics for Micro Air Vehicle Applications*, ser. Progress in Aeronautics and Astronautics. American Institute of Aeronautics and Astronautics (AIAA) Reston VA, 2001, no. 195.
- [55] N. Nguyen and I. Tuzcu, “Flight dynamics of flexible aircraft with aeroelastic and inertial force interactions,” in *Proc. AIAA Atmospheric Flight Mechanics Conference, Chicago, IL*, 2009, AIAA Paper 2009–6045.
- [56] B. Obradovic and K. Subbarao, “Modeling of dynamic loading of morphing wing aircraft,” in *Proc. AIAA Atmospheric Flight Mechanics Conference 2010, Toronto, ON, Canada*, 2010, AIAA Paper 2010–8236.
- [57] M. Ol, G. Parker, G. Abate, and J. Evers, “Flight controls and performance challenges for MAVs in complex environments,” in *Proc. AIAA Guidance, Navigation and Control Conference, Honolulu, HI*, 2008, AIAA Paper 2008–6508.
- [58] B. N. Pamadi, *Performance, Stability, Dynamics, and Control of Airplanes*, ser. AIAA Education Series. AIAA Reston VA, 1998.
- [59] B. N. Pamadi and L. W. Taylor Jr, “Estimation of aerodynamic forces and moments on a steadily spinning airplane,” *Journal of Aircraft*, vol. 21, no. 2, pp. 943 – 954, 1984.
- [60] A. Paranjape, E. Xargay, N. Hovakimyan, and C. Cao, “Adaptive controller for nonlinear strict feedback systems,” in *Proceedings of Mediterranean Conference on Control and Automation, Thessaloniki, Greece*, 2009, pp. 229–234.
- [61] A. A. Paranjape and N. Ananthkrishnan, “Combat aircraft agility metrics - a review,” *Journal of Aerospace Sciences and Technologies*, vol. 58, no. 2, pp. 1 – 16, 2006.

- [62] A. A. Paranjape, S.-J. Chung, H. H. Hilton, and A. Chakravarthy, “Dynamics and performance of a tailless MAV with flexible articulated wings,” *AIAA Journal*, 2011, to appear.
- [63] A. A. Paranjape, S.-J. Chung, and M. Krstic, “PDE boundary control for flexible articulated wings on a robotic aircraft,” *IEEE Transactions on Robotics*, 2011, in review, also available as AIAA Paper 2011-6486.
- [64] A. A. Paranjape, S.-J. Chung, and M. S. Selig, “Flight mechanics of a tailless articulated wing aircraft,” *Bioinspiration & Biomimetics*, vol. 6, no. 2, 2011.
- [65] A. A. Paranjape, N. K. Sinha, and N. Ananthkrishnan, “Use of bifurcation and continuation methods for aircraft trim and stability analysis - a state-of-the-art,” *Journal of Aerospace Sciences and Technologies*, vol. 60, no. 2, pp. 1 – 12, 2008.
- [66] V. Patel, C. Cao, N. Hovakimyan, K. Wise, and E. Lavretsky, “ \mathcal{L}_1 adaptive controller for tailless unstable aircraft in the presence of unknown actuator failures,” *International Journal of Control*, vol. 82, no. 4, pp. 705 – 720, 2009.
- [67] M. J. Patil and D. H. Hodges, “Flight dynamics of highly flexible flying wings,” *Journal of Aircraft*, vol. 43, no. 6, pp. 1790 – 1798, 2006.
- [68] D. A. Peters, S. Karunamoorthy, and W. M. Cao, “Finite state induced flow models part I: Two-dimensional thin airfoil,” *Journal of Aircraft*, vol. 32, no. 2, pp. 313 – 322, 1995.
- [69] A. P. Poppen Jr, “A method for estimating the rolling moment due to spin rate for arbitrary planform wings,” NASA TM-86365, 1985.
- [70] M. D. Queiroz, D. M. Dawson, M. Agarwal, and F. Zhang, “Adaptive nonlinear boundary control of a flexible link robotic arm,” *IEEE Trans. Robotics and Automation*, vol. 15, no. 4, pp. 779–787, 1999.
- [71] B. Raghavan and M. J. Patil, “Flight dynamics of high-aspect-ratio flying wings: Effect of large trim deformation,” *Journal of Aircraft*, vol. 46, no. 5, pp. 1808 – 1812, 2009.
- [72] —, “Flight control for flexible, high-aspect-ratio flying wings,” *Journal of Guidance, Control, and Dynamics*, vol. 33, no. 1, pp. 64 – 74, 2010.
- [73] P. K. Raghavendra, T. Sahai, P. A. Kumar, M. Chauhan, and N. Ananthkrishnan, “Aircraft spin recovery, with and without thrust vectoring, using nonlinear dynamic inversion,” *Journal of Aircraft*, vol. 42, no. 6, pp. 1492 – 1503, 2005.
- [74] M. Rais-Rohani, R. T. Haftka, B. Grossman, and E. R. Unger, “Integrated aerodynamic-structural-control wing design,” *Computing Systems in Engineering*, vol. 3, no. 6, pp. 639 – 650, 1992.
- [75] J. A. Ramsey, R. T. Ratliff, K. A. Wise, and E. Lavretsky, “Departure resilient control for autonomous air vehicles,” in *Proc. 2009 American Control Conference, St. Louis, MO*, 2009, pp. 5386 – 5391.

- [76] G. W. Reich, O. Wojnar, and R. Albertani, “Aerodynamic performance of a notional perching MAV design,” in *Proc. AIAA Aerospace Sciences Meeting and Exhibit, Orlando, FL*, 2009, AIAA Paper 2009–63.
- [77] W. P. Rodden, “Dihedral effect of a flexible wing,” *Journal of Aircraft*, vol. 2, no. 5, pp. 368 – 373, 1965.
- [78] D. L. Russell, “Controllability and stabilizability theory for linear partial differential equations: Recent progress and open questions,” *SIAM Review*, vol. 20, no. 4, pp. 639 – 739, 1978.
- [79] G. Sachs, “What can be learned from unique lateral-directional dynamics properties of birds for mini-aircraft,” in *Proc. AIAA Atmospheric Flight Mechanics Conference 2007, Hilton Head, SC*, 2007, AIAA Paper 2007–6311.
- [80] —, “Why birds and miniscale airplanes need no vertical tail,” *Journal of Aircraft*, vol. 44, no. 4, pp. 1159 – 1167, 2007.
- [81] G. Sachs and F. Holzapfel, “Flight mechanic and aerodynamic aspects of extremely large dihedral in birds,” in *Proc. AIAA Aerospace Sciences Meeting and Exhibit 2007, Reno, NV*, 2007, AIAA Paper 2007–46.
- [82] D. Salamon, “Realization theory in hilbert space,” *Mathematical Systems Theory*, vol. 21, pp. 147 – 164, 1989.
- [83] M. S. Selig, “Modeling full-envelope aerodynamics of small UAVs in realtime,” in *Proc. AIAA Atmospheric Flight Mechanics Conference, Toronto, ON, Canada*, 2010, AIAA Paper 2010–7635.
- [84] —, “Modeling propeller aerodynamics and slipstream effects on small UAVs in realtime,” in *Proc. AIAA Atmospheric Flight Mechanics Conference, Toronto, ON, Canada*, 2010, AIAA Paper 2010–7938.
- [85] C. M. Shearer and C. E. S. Cesnik, “Nonlinear flight dynamics of very flexible aircraft,” *Journal of Aircraft*, vol. 44, no. 5, pp. 1528 – 1545, 2007.
- [86] Y. Shtessel, J. Buffington, and S. Banda, “Tailless aircraft flight control using multiple time scale reconfigurable sliding modes,” *IEEE Trans. Control Systems Technology*, vol. 10, no. 2, pp. 288 – 296, 2002.
- [87] W. Shyy, H. Aono, S. K. Chimakurthi, P. Trizila, C.-K. Kang, C. E. S. Cesnik, and H. Liu, “Recent progress in flapping wing aerodynamics and aeroelasticity,” *Progress in Aerospace Sciences*, vol. 46, pp. 284 – 327, 2010.
- [88] A. A. Siranosian, M. Krstic, A. Smyshlyaev, and M. Bememt, “Gain scheduling-inspired boundary control for nonlinear partial differential equations,” *Journal of Dynamic Systems, Measurement, and Control*, vol. 133, no. 051007, 2011.
- [89] S. A. Snell, D. F. Enns, and W. L. G. Jr, “Nonlinear inversion flight control for a supermaneuverable aircraft,” *Journal of Guidance, Control, and Dynamics*, vol. 15, no. 4, pp. 976 – 984, 1992.

- [90] A. Song, X. D. Tian, E. Israeli, R. Galvao, K. Bishop, S. Swartz, and K. Breuer, “Aeromechanics of membrane wings with implications for animal flight,” *AIAA Journal*, vol. 46, no. 8, pp. 2096 – 2106, 2008.
- [91] L. Squire, D. Berg, F. Bloom, S. du Lac, A. Ghosh, and N. Spitzer, *Fundamental Neuroscience*. Elsevier Inc., 2008.
- [92] G. Stenfelt and U. Ringertz, “Lateral stability and control of a tailless aircraft configuration,” *Journal of Aircraft*, vol. 46, no. 6, pp. 2161 – 2163, 2009.
- [93] ———, “Yaw control of a tailless aircraft configuration,” *Journal of Aircraft*, vol. 47, no. 5, pp. 1807 – 1810, 2010.
- [94] R. H. Stone, “Aerodynamic modeling of the wing-propeller interaction for a tail-sitter unmanned air vehicle,” *Journal of Aircraft*, vol. 45, no. 1, pp. 198 – 210, 2008.
- [95] S. Strogatz, *Nonlinear Dynamics and Chaos With Applications to Physics, Biology, Chemistry, and Engineering*. Cambridge, MA: Perseus Books Group, 1994.
- [96] W. Su and C. E. S. Cesnik, “Nonlinear aeroelasticity of a very flexible blended-wing-body aircraft,” *Journal of Aircraft*, vol. 47, no. 5, pp. 1539 – 1553, 2010.
- [97] T. Theodorsen, “General theory of aerodynamic instability and the mechanism of flutter,” NACA Report 496, 1935.
- [98] A. L. R. Thomas and G. K. Taylor, “Animal flight dynamics i. stability in gliding flight,” *Journal of Theoretical Biology*, vol. 212, pp. 399 – 424, 2001.
- [99] D. T. Tran and R. Lind, “Parameterizing stability derivatives and flight dynamics with wing deformation,” in *AIAA Atmospheric Flight Mechanics Conference 2010*, 2010, AIAA Paper 2010–8227.
- [100] D. Uhlig, A. Sareen, P. Sukumar, A. Rao, and M. S. Selig, “Determining aerodynamic characteristics of a micro air vehicle using motion tracking,” in *Proc. AIAA Atmospheric Flight Mechanics Conference, Toronto, ON, Canada*, 2010, AIAA Paper 2010–8416.
- [101] M. W. Vandegrift, F. L. Lewis, and S. Q. Zhu, “Flexible-link robot arm control by a feedback linearization/singular perturbation approach,” *Journal of Robotic Systems*, vol. 11, no. 7, pp. 591 – 603, 1994.
- [102] R. Vazquez and M. Krstic, “A closed-form feedback controller for stabilization of the linearized 2-D Navier-Stokes Poiseuille system,” *IEEE Transactions on Automatic Control*, vol. 52, no. 12, pp. 2298 – 2312, 2007.
- [103] Q. Wang and R. F. Stengel, “Robust nonlinear flight control of a high-performance aircraft,” *IEEE Trans. Control Systems Technology*, vol. 13, no. 1, pp. 15 – 26, 2005.
- [104] M. R. Waszak and D. K. Schmidt, “Flight dynamics of aeroelastic vehicles,” *Journal of Aircraft*, vol. 25, no. 6, pp. 563 – 571, 1988.

- [105] A. Wickenheiser and E. Garcia, “Longitudinal dynamics of a perching aircraft,” *Journal of Aircraft*, vol. 43, no. 5, pp. 1386 – 1392, 2006.
- [106] —, “Optimization of perching maneuvers through vehicle morphing,” *Journal of Guidance, Control and Dynamics*, vol. 31, no. 4, pp. 815 – 823, 2008.
- [107] R. J. Wood, “The first takeoff of a biologically inspired at-scale robotic insect,” *IEEE Transactions on Robotics*, vol. 24, no. 2, pp. 341 – 347, 2008.
- [108] J. R. Wright and J. E. Cooper, *Introduction to Aircraft Aeroelasticity and Loads*, ser. Aerospace Series. John Wiley & Sons, England, 2007.